



MINISTÉRIO DA CIÊNCIA, TECNOLOGIA, INOVAÇÕES E COMUNICAÇÕES  
**INSTITUTO NACIONAL DE PESQUISAS ESPACIAIS**

sid.inpe.br/mtc-m21c/2019/04.01.16.07-TDI

## PHYSICAL LIMNOLOGY OF LARGE FLOODPLAIN LAKES ALONG THE LOWER AMAZON RIVER

Pétala Bianchi Augusto Silva

Doctorate Thesis of the Graduate Course in Remote Sensing, guided by Drs. Evlyn Márcia Leão de Moraes Novo, and Conrado de Moraes Rudorff, approved in April 09, 2019.

URL of the original document:

<<http://urlib.net/8JMKD3MGP3W34R/3T3DDKS>>

INPE  
São José dos Campos  
2019

**PUBLISHED BY:**

Instituto Nacional de Pesquisas Espaciais - INPE  
Gabinete do Diretor (GBDIR)  
Serviço de Informação e Documentação (SESID)  
CEP 12.227-010  
São José dos Campos - SP - Brasil  
Tel.:(012) 3208-6923/7348  
E-mail: pubtc@inpe.br

**BOARD OF PUBLISHING AND PRESERVATION OF INPE  
INTELLECTUAL PRODUCTION - CEPPII (PORTARIA N°  
176/2018/SEI-INPE):****Chairperson:**

Dra. Marley Cavalcante de Lima Moscati - Centro de Previsão de Tempo e Estudos  
Climáticos (CGCPT)

**Members:**

Dra. Carina Barros Mello - Coordenação de Laboratórios Associados (COCTE)  
Dr. Alisson Dal Lago - Coordenação-Geral de Ciências Espaciais e Atmosféricas  
(CGCEA)  
Dr. Evandro Albiach Branco - Centro de Ciência do Sistema Terrestre (COCST)  
Dr. Evandro Marconi Rocco - Coordenação-Geral de Engenharia e Tecnologia  
Espacial (CGETE)  
Dr. Hermann Johann Heinrich Kux - Coordenação-Geral de Observação da Terra  
(CGOBT)  
Dra. Ieda Del Arco Sanches - Conselho de Pós-Graduação - (CPG)  
Sílvia Castro Marcelino - Serviço de Informação e Documentação (SESID)

**DIGITAL LIBRARY:**

Dr. Gerald Jean Francis Banon  
Clayton Martins Pereira - Serviço de Informação e Documentação (SESID)

**DOCUMENT REVIEW:**

Simone Angélica Del Ducca Barbedo - Serviço de Informação e Documentação  
(SESID)  
André Luis Dias Fernandes - Serviço de Informação e Documentação (SESID)

**ELECTRONIC EDITING:**

Ivone Martins - Serviço de Informação e Documentação (SESID)  
Cauê Silva Fróes - Serviço de Informação e Documentação (SESID)



MINISTÉRIO DA CIÊNCIA, TECNOLOGIA, INOVAÇÕES E COMUNICAÇÕES  
**INSTITUTO NACIONAL DE PESQUISAS ESPACIAIS**

sid.inpe.br/mtc-m21c/2019/04.01.16.07-TDI

## PHYSICAL LIMNOLOGY OF LARGE FLOODPLAIN LAKES ALONG THE LOWER AMAZON RIVER

Pétala Bianchi Augusto Silva

Doctorate Thesis of the Graduate Course in Remote Sensing, guided by Drs. Evlyn Márcia Leão de Moraes Novo, and Conrado de Moraes Rudorff, approved in April 09, 2019.

URL of the original document:

<<http://urlib.net/8JMKD3MGP3W34R/3T3DDKS>>

INPE  
São José dos Campos  
2019

Cataloging in Publication Data

---

Augusto-Silva, Pétala Bianchi.

Au45p Physical limnology of large floodplain lakes along the lower Amazon river / Pétala Bianchi Augusto Silva. – São José dos Campos : INPE, 2019.

xxiv + 91 p. ; (sid.inpe.br/mtc-m21c/2019/04.01.16.07-TDI)

Thesis (Doctorate in Remote Sensing) – Instituto Nacional de Pesquisas Espaciais, São José dos Campos, 2019.

Guiding : Drs. Evlyn Márcia Leão de Moraes Novo, and Conrado de Moraes Rudorff.

1. Tropical shallow floodplain lakes. 2. Mixing. 3. Convective cooling. 4. Water surface temperature. 5. Remote sensing. I.Title.

CDU 528.8:551.435.12(811)

---



Esta obra foi licenciada sob uma Licença [Creative Commons Atribuição-NãoComercial 3.0 Não Adaptada](https://creativecommons.org/licenses/by-nc/3.0/).

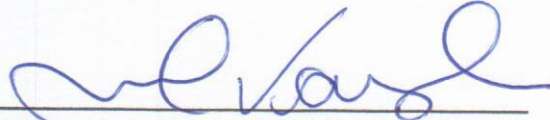
This work is licensed under a [Creative Commons Attribution-NonCommercial 3.0 Unported License](https://creativecommons.org/licenses/by-nc/3.0/).

Aluno (a): **Pétala Bianchi Augusto Silva**

Título: "PHYSICAL LIMNOLOGY OF LARGE FLOODPLAIN LAKES ALONG THE LOWER AMAZON RIVER"

Aprovado (a) pela Banca Examinadora em cumprimento ao requisito exigido para obtenção do Título de **Doutor(a)** em **Sensoriamento Remoto**

Dr. Milton Kampel



Presidente / INPE / SJCampos - SP

( ) Participação por Vídeo - Conferência

Aprovado ( ) Reprovado

Dra. Evelyn Márcia Leão de Moraes Novo



Orientador(a) / INPE / SJCampos - SP

( ) Participação por Vídeo - Conferência

Aprovado ( ) Reprovado

Dr. Conrado de Moraes Rudorff

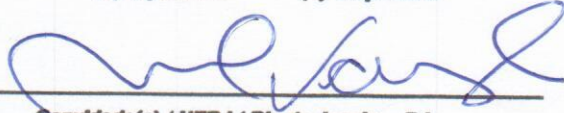


Orientador(a) / CEMADEN / São José dos Campos - SP

( ) Participação por Vídeo - Conferência

Aprovado ( ) Reprovado

Dr. Lino Augusto Sander de Carvalho

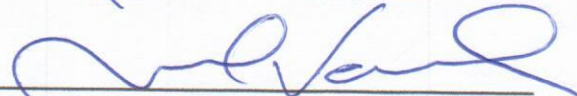


Convidado(a) / UFRJ / Rio de Janeiro - RJ

Participação por Vídeo - Conferência

Aprovado ( ) Reprovado

Dr. John Michael Melack



Convidado(a) / Univ. of California / United States of America - USA

Participação por Vídeo - Conferência

Aprovado ( ) Reprovado

Este trabalho foi aprovado por:

( ) maioria simples

unanimidade

São José dos Campos, 09 de abril de 2019



*"The image of the world is only half of the world".*

*C. G. Jung*



To my mom, who wanted to be another kind of “doctor”. To my dad, who brought me here. To my aunt, who can’t be physically here. To me, because it hurts.



## ACKNOWLEDGEMENTS

Como diria Emicida (a quem agradeço muito): “eu tô pra ver sangrar o que eu sangrei”. Eu sangrei. Esse doutorado teve de tudo: de mortes a golpe de estado, de separação a crises de pânico, de acidente de carro a duas dengues, três apartamentos diferentes, cinco cidades diferentes, *Burnout* ... A lista é grande e continua e o mundo precisa saber que o doutorado faz parte de uma vida, mas não se torna a vida da pessoa, o que não deveria acontecer. A vida de ninguém para pra esperar o fim de um doutorado. As vezes as pessoas pausam suas vidas por alguma meta, esperam concluir alguns ciclos pra começarem a “viver”. As vezes essa vida pode nunca começar e eu vi isso acontecer vezes demais pra minha idade.

Eu dei o meu máximo. Eu cheguei no meu limite físico. Pra muitas pessoas isso pode não ser o suficiente, mas foi o que eu consegui. Devo isso a algumas pessoas muito importantes: meus pais e tios por me pressionarem pra terminar; a Mila por entender cada lágrima, conversar, aguentar desabafos, discutir e dar ideias; ao Celso por ter me inspirado; ao Renato pela ajuda e companhia; ao Lino pelos conselhos, questionamentos e etc.; à Alessandra, pelo acompanhamento psicológico; ao Stech, pelo carinho; ao Kadu por não me deixar sem sustento; aos amigos do Poliedro pela força; às mulheres bruxas da minha vida Patrícia, Cíntia, Thaíses, Ariane, Cioni, Debs, Mila, Fabi, Sílvia, Adriana, Rose... vocês me fizeram mais forte; aos meus guias, pois eu sou uma mera trabalhadora; ao Rapha, pois não me esquecerei daquela sexta-feira às vésperas de entregar esse documento.

Um agradecimento mais que especial aos meus orientadores, Evlyn e Conrado, pela oportunidade e por todo suporte diante das crises pelas quais passei nesses anos. Eu sinto muito se não atendi ao que eu mesma achava que conseguiria.

Agradeço também ao John e à Sally pela disposição e generosidade e à Alicia pela ajuda sempre tão rápida.

Agradeço ao curso de Pós-Graduação em Sensoriamento Remoto através da figura magnífica de sua coordenadora, Dra. Ieda, e ao apoio da Coordenação de Aperfeiçoamento de Pessoal de Nível Superior - Brasil (CAPES) – pelo código de financiamento 001. Agradeço também à Fundação de Amparo à Pesquisa do Estado de São Paulo (FAPESP) e ao Conselho Nacional de Desenvolvimento Científico e Tecnológico (CNPq) pelo apoio financeiro a essa pesquisa pelos subsídios #2011/23594-8 e #304568/2014-7, respectivamente.

## ABSTRACT

Large, shallow lakes are common in the extensive floodplains throughout the tropics and its importance for climate regulation has already been proven. To determine controls on their mixing dynamics in order to help define proper simplifications to insert this type of lakes in land surface models, five stations were instrumented with meteorological and temperature sensors and placed in two shallow connected tropical lakes on the lower Amazon floodplain. A tight relation between changes in thermal structure and  $L_{MO}/h$  (the ratio of the Monin-Obukhov length scale –  $L_{MO}$  – to the depth of the actively mixing layer –  $h$ ) indicates the sensitivity of thermal structure to wind speed relative to heating and cooling. Four regimes led to variations in mixing: (i) high solar radiation with light winds in the mid-morning to early afternoon resulted in shallow stratification,  $0 < L_{MO}/h < 1$ ; (ii) afternoons with higher winds caused the diurnal thermocline to downwell and heat to mix to deeper layers,  $L_{MO}/h > 1$ ; (iii) by late afternoon, buoyancy flux became negative and  $L_{MO}/h < -1$  and with  $u_{*W}$  and  $w_*$  both  $> 0.06 \text{ m}\cdot\text{s}^{-1}$ , mixing from wind and cooling co-occurred; and (iv) convection dominated mixing on nights with light winds,  $-1 < L_{MO}/h < 0$ . Pattern (ii) occurred mid-day if winds were higher. When winds were intermittent and regime (i) predominated mid-day, changes in heat content were primarily determined by one-dimensional processes of heating and cooling. When easterly winds were sustained and regime (ii) occurred mid-day, heat was transported west in the day, and colder water upwelled to the west or was advected to the west and north at night. Subtle differences in wind speed

determined the extent to which advection moderated the thermal structure. Wind and solar radiation were found to be the most important parameters influencing the water column thermal structure of the lakes under study. Given the regimes identified by the *in situ* measurements and the increasingly applicability of orbital remote sensing to the study of the temperature patterns on inland aquatic systems, a model was developed for extracting bulk temperature (equivalent to that measured *in situ*) from the surface temperature (called skin temperature) provided by the MOD11A1 product of the MODIS sensor onboard the Aqua and Terra satellites. This model was calibrated and validated using a Monte Carlo simulation, resulting in a normalized error of 18.32%. The model, however, presented low  $R^2$  values, indicating that further research is needed on longer time series before this product can be used for pattern studies.

**Keywords:** Tropical shallow floodplain lakes; mixing; convective cooling; wind; advection; water surface temperature; remote sensing.

# LIMNOLOGIA FÍSICA DE GRANDES LAGOS DE PLANÍCIE DE INUNDAÇÃO AO LONGO DO BAIXO RIO AMAZONAS

## RESUMO

Grandes lagos rasos são comuns nas extensas planícies de inundação ao longo dos trópicos cuja importância para a regulação climática já foi comprovada na literatura científica. Para determinar os fatores que controlam a dinâmica de mistura desses lagos e contribuir para a definição de simplificações mais adequadas para inserção desse tipo de lagos em modelos de superfície, cinco estações foram instrumentadas com sensores meteorológicos e de temperatura e posicionadas em dois lagos rasos interconectados da planície de inundação do baixo Amazonas. Uma relação estreita entre as variações da estrutura térmica da coluna d'água e a razão  $L_{MO}/h$  (razão da escala de comprimento de Monin-Obukhov –  $L_{MO}$  – pela profundidade da camada de mistura ativa –  $h$ ) indica sensibilidade da estrutura térmica em relação à velocidade do vento. Quatro regimes conduzem a variações na mistura da coluna d'água desses lagos: (i) a alta incidência de radiação solar e vento leve do meio da manhã até o início da tarde resulta em estratificação rasa, próxima à superfície e com a razão entre  $0 < L_{MO}/h < 1$ ; (ii) o vento mais forte à tarde causou o aprofundamento da termoclina diurna, o que resultou em calor sendo levado às camadas mais profundas e a razão  $L_{MO}/h > 1$ ; (iii) ao final da tarde, o fluxo de fluatibilidade tornou-se negativo levando a razão a  $L_{MO}/h < -1$  e, com ambas velocidades horizontal ( $u_{*W}$ ) e vertical ( $w_*$ ) de

fricção da água maiores que  $0.06 \text{ m.s}^{-1}$ , a mistura devido ao vento e aquela devido ao resfriamento da água ocorreram simultaneamente; e (iv) a convecção dominou a mistura da coluna d'água em noites com vento leve e, com isso, a razão ficou  $-1 < L_{MO}/h < 0$ . O regime (ii) ocorreu ao meio dia caso o vento fosse mais forte. Quando o vento era intermitente e o regime (i) predominava ao meio dia, mudanças no conteúdo de calor na coluna d'água eram determinadas por processos de resfriamento e aquecimento em uma dimensão apenas. Quando ventos orientais eram mantidos e o regime (ii) ocorria ao meio dia, o calor era transportado para oeste durante o dia, fazendo com que águas mais frias emergissem ou fossem transportadas para essa região dos lagos à noite. Diferenças súbitas na velocidade do vento determinaram a extensão com que a advecção impactava a estrutura térmica. Vento e radiação solar foram os parâmetros mais importantes de regulação da estrutura térmica da coluna d'água dos lagos estudados. Tendo em vista os regimes identificados pelas medidas *in situ* e a crescente aplicação do sensoriamento remoto orbital ao estudo dos padrões de temperatura de sistemas aquáticos continentais, desenvolveu-se um modelo para a estimativa da temperatura volumétrica (equivalente àquela medida *in situ*) a partir da temperatura de superfície (*skin temperature*) fornecidas pelo produto MOD11A1 do sensor MODIS a bordo dos satélites Aqua e Terra. Esse modelo foi calibrado e validado utilizando-se uma simulação Monte Carlo, resultando em erro normalizado de 18.32 %. O modelo, contudo, apresentou valores baixos de  $R^2$ , indicando que são necessárias pesquisas mais aprofundadas em

séries temporais mais longas antes que possam ser usados para levantamento de padrões.

**Palavras-chave:** Lagos rasos de planície de inundação tropical; mistura; resfriamento convectivo; vento; advecção; temperatura da superfície da água; sensoriamento remoto.



## LIST OF FIGURES

**Pág.**

Figure 2.1: Study site. (a) The Amazon basin and the study site location. (b) True color Landsat 8 composite (date: 07/17/2014) of Curuai floodplain and location of the field measurements. Detail of the distribution of the: (c) thermistor chains; (d) wind buoys and meteorological station (buoy 2); and (e) discrimination of the lakes studied. ....	8
Figure 3.1: Thermistor chain structure.....	13
Figure 4.1: Five-minute averages of meteorological data from station 2: (a) air temperature and near-surface water temperature; (b) shortwave incoming radiation (SW); (c) wind speed (WS); (d) wind direction (WD); and (e) relative humidity (RH).....	24
Figure 4.2: (a) Hourly time series of components of the surface energy budget: sensible heat flux (SE), latent heat flux (LE), and net longwave radiation ( $LW_{Net}$ ); (b) Surface heat flux (blue line) and effective heat flux (green line) into the actively mixing layer; and (c) Buoyancy flux. ....	27
Figure 4.3: (a) Water friction ( $u_{*W}$ , blue line) and penetrative convection velocity ( $w_*$ , green line); and (b) Half hour averaged turbulent energy flux into the actively mixing layer ( $F_q$ ) (blue, left axis) and the ratio $0.5w_*^3 : F_q$ (green, right axis). Computed for station 2 except on days 174 to late afternoon on day 177 when the gaps were filled using computations from Station 1. ....	29
Figure 4.4: Ratio between penetrative convection velocity and water shear velocity. Red line represents equals do one.....	30
Figure 4.5: $L_{MO}$ in the water (cool in blue, heat in red) and h (black line) with subpanels ordered from station 1 (S1) to station 5 (S5). ....	32

Figure 4.6: Top panel: Hourly averages of  $L_{MO}/h$  for station 1, first three days, and station 2 thereafter, and lower panels: Time-depth diagrams of water temperature for: (a) days 174-180 and (b) days 181-187. Subpanels are ordered from station 1 to station 5. Isotherms are every 0.1°C below 29°C (white) and every 0.2°C above that temperature (black). Positive values of  $LMO/h$  indicate heating, and the ratio equals fraction of the actively mixing layer mixed by wind. Red dots indicate the thermistor positions for each chain. Upper three thermistors on chain 2 were lost after initial deployment and replaced on day 178. .... 34

Figure 4.7: Summary of the periods identified by ratio  $LMO/h$ .....36

Figure 4.8: Five-minute time series of (a) wind direction (WD, blue, left axis) and effective heat flux into the actively mixing layer (HF, green, right axis); (b) wind speed (WS); and (c) time-depth diagram of buoyancy frequency (N) in cycles per hour (cph) for days 181 to 184 at station 2. The white line marks the depth of the actively mixing layer, the magenta and dashed black-white lines show  $L_{MO}$  under cooling and heating, respectively..... 38

Figure 4.9: Relation between the buoyancy frequency (N, in cph) and  $F_q$  during heating between late morning and mid-afternoon (i.e., 9:30 to 14:30) when the ratio  $L_{MO}/h$  is (a)  $0 < L_{MO}/h < 1$  when light winds yield strong and shallow stratification, and (b)  $L_{MO}/h > 1$  when strong winds caused the weakening of the stratification from downwelling of the diurnal thermocline and near surface mixing. .... 40

Figure 4.10:  $Q_M$  (green line) and  $Q_T$  (blue line) for stations (S) 1 to 5. Data are filtered over 2 hours..... 42

Figure 4.11: Example from station 2: (a) Wind Speed (WS) and Wind Direction (WD); (b) Isotherms where blue lines indicate upwelling; and (c)  $Q_M$  (green line) and  $Q_T$  (blue line)..... 44

Figure 4.12: (a) Transect in the main wind direction from station 3 (S3) to station 5 (S5) showing the main components of the heat budget. Arrows coming from the bottom towards the surface layer represent the upwelling of cold water from the hypolimnion as the wind is tilting the thermocline in the main wind direction (from East to West); (b) Temperature profiles for Stations 3 and 5 at 13:00 (local time). ..... 45

Figure 4.13: (a) Hourly heat content per unit area estimated from temperature in the water column,  $Q_T$  (blue line), and computed using meteorological data,  $Q_M$  (green line) at station 3. (b) Anomalies between the observed heat content in the lake and that predicted from meteorological data ( $Q_T - Q_M$ ) at stations 2 and 3 (blue and green, respectively); (c) As in panel b except for stations 4 and 5..... 46

Figure 5.1: Flowchart of the calibration/validation of the WST model using a Monte Carlo simulation. .... 64

Figure 5.2: WST from all sampling stations from day 175 to the end of day 180..... 66

Figure 5.3: WST from all sampling stations from day 181 to the end of day 186..... 67

Figure 5.4: WST measured in situ ( $WST_i$  black marks) and measured by MODIS ( $WST_M$  red dots-no model applied) from all sampling stations from day 174 until day 188. .... 68

Figure 5.5:  $WST_i$  and  $WST_{est}$  separated by sampling Stations (S#, represent the station and its number). Blue dashed line represents 1:1 between measured and estimated temperatures ..... 71



## LIST OF TABLES

	<u>Pág.</u>
Table 2.1: Lake depth, diffuse light attenuation coefficient ( $K_d$ PAR) and fetch at the field sampling stations. Fetch was measured from east to west on the Landsat 8 image acquired on June 17, 2014. Lake depth and $K_d$ were measured during the field campaign.....	9
Table 4.1: Result of the histograms of the ratio $0.5W_*^3 : F_q$ in all stations. ....	31
Table 5.1: Summary of the error estimators used. Where: $y_i$ and $x_i$ are $WST_M$ and $WST_i$ respectively in each $i$ sample. ....	64
Table 5.2: Coefficients derived from the calibration/validation scheme. ....	70
Table 5.3: Mean $WST_i - WST_{Est}$ for each Station. ....	70



## CONTENT

	<u>Pág.</u>
1 INTRODUCTION .....	1
2 STUDY SITE.....	7
3 FIELD MEASUREMENTS .....	11
4 STRATIFICATION AND MIXING IN LARGE FLOODPLAIN LAKES ALONG THE LOWER AMAZON RIVER.....	15
4.1 Methods.....	18
4.1.1 Surface energy budget, turbulent velocity scales, and heat budgets .....	18
4.1.2 Length of Monin-Obukhov ( $L_{mo}$ ).....	21
4.1.3 Stratification and the depth of the actively mixing layer .....	22
4.1.4 Advection.....	23
4.2 Results.....	23
4.2.1 Meteorology .....	23
4.2.2 Turbulent velocity scales.....	27
4.2.3 The Length of Monin-Obukhov ( $L_{MO}$ ) in the water and the actively mixing layer (h) .....	31
4.2.3.1 Nocturnal pattern.....	32
4.2.3.2 Diurnal pattern.....	33
4.2.4 Thermal stratification.....	33
4.2.5 Local changes in heat content versus changes from advection.....	41
4.3 Discussion .....	47
4.3.1 Nocturnal convection .....	52
4.3.2 Biological and biogeochemical implications.....	54
5 ASSESSING REMOTE SENSING APPLICABILITY FOR EXTRACTING DIRECT ESTIMATES OF WST IN FLOODPLAIN LAKES OF THE LOWER AMAZON RIVER AT HIGH DISCHARGE ...	57
5.1 Methods.....	61
5.1.1 <i>In situ</i> measurements of WST.....	61
5.1.2 Remote sensing of WST .....	62
5.1.3 Calibration/Validation of the empirical model.....	62

5.2	Results.....	65
5.2.1	Meteorology .....	65
5.2.2	Water surface temperature patterns .....	66
5.2.3	Calibration/Validation of remote sensing data.....	69
5.2.4	Bulk temperature estimated by MODIS.....	70
5.3	Discussion .....	71
6	CONCLUSIONS .....	75
	REFERENCES.....	79

## 1 INTRODUCTION

Mixing patterns have been extensively studied in lakes of the boreal and temperate regions (EUGSTER et al., 2003; EVANS et al., 2008; MACINTYRE et al., 2009; MACINTYRE et al., 2010; READ et al., 2012; TEDFORD et al., 2014; HEISKANEN et al., 2014, PERNICA et al. 2014). These lakes undergo strong seasonal variations in solar radiation and air temperature (MACINTYRE; MELACK, 2009). Tropical floodplain lakes, in contrast, are subjected to less seasonality in meteorological variables, but are strongly influenced by flooding from the main river, i.e. water stage, which alters conditions of lake morphometry, magnitude, direction and distribution of advective flows, light attenuation and distribution of flooded vegetation.

Previous studies characterized thermal stratification in the water column of small floodplain lakes in the central Amazon (LAKE CALADO; LAKE JANAUCÁ – MELACK; FISHER, 1983; MACINTYRE; MELACK, 1984; LAKE CRISTALINO; LAKE JACARETINGA – TUNDISI et al., 1984) and reached similar conclusions regarding mixing patterns. The effects of physical forces (e.g., wind, solar radiation, evaporation) are modified by lakes' surface area and depth, varying seasonally and spatially. During rising and receding water stages, lakes are likely to be vertically mixed at sunrise, develop a shallow thermocline (~0.5 m) towards mid-day at low wind conditions, and fully mix again at night. During the high-water stage, lakes may develop periods of stable stratification under low wind conditions with significant diel variation of the mixed layer depth (1 to 6 m, depth permitting). Large wind fetches will increase vertical and horizontal mixing.

Engle and Melack (2000) and Caraballo et al. (2014) studied lakes with persistent stratification during high water, which was interrupted during *friagem* events. *Friagem* is a cold front displacement from the south. It normally occurs between May and August (high-water phase in Central Amazon) and lead to strong winds and sudden temperature drop. The authors point out that, with a combination of low air temperature, low incident radiation and strong, persistent wind, complete mixing is possible even during high water. Therefore, in lakes with large fetch and persistent wind, the hypothesis of complete mixing at diel time scales even during high water stage, with depths deeper than 5 m, is realistic.

Melo et al. (2004) studied the density and vertical distribution of phytoplankton during high water in two small Amazon floodplain lakes, Lake Batata and Lake Mussurá, both formed by Trombetas River and located on lower Amazon floodplain. Those lakes, despite both being 8 m deep, had different mixing patterns. Lake Batata was subjected to complete diel mixing and had scarce phytoplankton community, homogeneously distributed in the water column at the end of the night. Lake Mussurá had a mixing depth and phytoplankton distribution restricted to 3 m with population densities higher than those of Lake Batata. The assumed reason for these differences relies on the advective fluxes from Trombetas River. These fluxes have larger influence on Lake Batata during high water phase whereas Lake Mussurá remains as a lentic system throughout the hydrological year due to the position of the lakes related to the connected river. Melo et al. (2004) illustrated the controls that mixing patterns

impose over the phytoplankton in the water column and the role of lateral advection over the vertical mixing patterns.

At lower reaches of the Amazon River, mixing patterns have not been analyzed. There, overbank deposition gradually buries scroll topography (MERTES et al. 1995), large shallow lakes are more abundant, smaller local catchment to lake area ratios dominates, and water level amplitude is lower than upstream. Though studies by Engle and Melack (2000), Melo et al. (2004) and Caraballo et al. (2014) indicate that complete mixing is possible even during high water stage, the physical forces that determine the occurrence of complete mixing events and the influences of lake morphometry and advective flows remain to be examined.

It is expected that lake area, lake physical properties and lake biogeochemistry will interact with climate change, especially due to climate warming. It can alter lake mixing regimes (MACKAY et al., 2009; WEYHENMEYER et al., 2017) and have feedbacks to regional climate. The impact of temperate and boreal lakes to regional climate have been demonstrated by Samuelsson et al. (2010) and Subin et al. (2012). Their work showed climate impacts related to the inclusion of lakes in land surface models coupled with climate models. Lakes influence local to regional climate due to their different albedo, higher heat conductance under the surface, higher effective heat capacity and lower surface roughness than surrounding land. Its importance to climate prediction and estimates of climate change impacts is unquestionable, still most general circulation models have, at best, simple and largely untested representations of lakes Subin et al. (2012). In addition to that, studies in the Amazon basin have demonstrated that

floodplains and associated lakes act as important regional sources and/or sinks of carbon (ENGLE; MELACK, 2000; RICHEY et al., 2002; MELACK et al., 2004; KEMENES et al., 2007; RUDORFF et al. 2011; MELACK; COE, 2013; ABRIL et al., 2014) and, given wetlands extent in the Amazon ( $8.4 \times 10^5 \text{ km}^2$ ; HESS et al., 2015), it is important to examine mixing patterns and the physical forces that control it in a class of lakes abundant in Amazon basin and other organic-rich floodplains in order to help understand the role of these lakes in the regional climate.

Aiming to solve the gaps raised above, the Chapter 4 of this thesis was dedicated to study the vertical thermal structure and mixing of Lago Paranaatinga ( $2^\circ 4' 15.93'' \text{S}$ ,  $55^\circ 40' 8.03'' \text{W}$ ) and Lago do Poço Grande ( $2^\circ 7' 59.47'' \text{S}$ ,  $55^\circ 38' 52.24'' \text{W}$ ). They comprise a floodplain of the Amazon River called Curuai floodplain, located at its southern margin, near the city of Óbidos, State of Pará. Both lakes have large wind fetch, which enables to test the hypothesis of complete mixing occurrence due to wind even during high-water stage.

Time series measurements of surface meteorology and water column thermal structure were acquired, together with measurements of light attenuation. Spatial and temporal variations in water thermal structure and surface meteorology of the area is described to identify dominant lake mixing processes at the diel timescale. Data were collected during high water stage, in a period of overbank flow of river water onto the floodplain, strong heating due to persistent incident solar radiation, and persistent wind forcing. Surface energy budget was quantified and used to determine the domains where wind stirring, convective

cooling due to heat losses and advective flows from other flooded environments caused mixed layer deepening. Vertical mixing patterns were analyzed, and they showed that horizontal overflows can influence the depth of the surface mixed layer and cause thermocline tilting and upwelling from the hypolimnion. With this set of data and calculations, it was possible to demonstrate the mixing patterns of a large tropical floodplain lake. The results demonstrated here may affect the representation of this class of lakes in land surface models and expand our understanding of processes of lake mixing in the tropics.

Given the results from Chapter 4 of this thesis, it was possible to define the physical forces that most greatly affect mixing patterns of the lakes under study: wind and water temperature (as result from incident radiation). Wind is a source of turbulent kinetic energy in the water column and it can be responsible for erosion of vertical temperature gradients. Water surface temperature (WST) in its turn, is a good indicator of climate change (ADRIAN et al., 2009; LIVINGSTONE, 2003; WEYHENMEYER et al., 2017). Due to its high heat capacity, small changes in water temperature can affect the duration of stratification (Augusto-Silva et al., 2019), the development of algal blooms and of oxygen depleted zones (LIVINGSTONE, 2003; SAHOO; SCHLADOW, 2008; BOUFFARD et al., 2013). WST is a necessary parameter for calculations of heat, momentum, and it determines the flux of gases such as carbon dioxide and methane between the water and the atmosphere (EMERY et al., 2001). Weyhenmeyer et al. (2017) have demonstrated that temperature difference between air and water can be used to evaluate whether the water body will

function as a source or a sink of greenhouse gases to the atmosphere and so proving the importance of this parameter to climate modeling.

Remote sensing capability for estimating wind still lacks the required spatial and temporal resolution to be applied to inland waterbodies studies, so the chosen most promising forcing to be estimated by remote sensing was water surface temperature (WST) and remote sensing applicability for estimating it was evaluated in Chapter 5. A model for estimating WST was developed and validated by relating *in situ* WST (bulk temperature) to MODIS skin layer temperature directly.

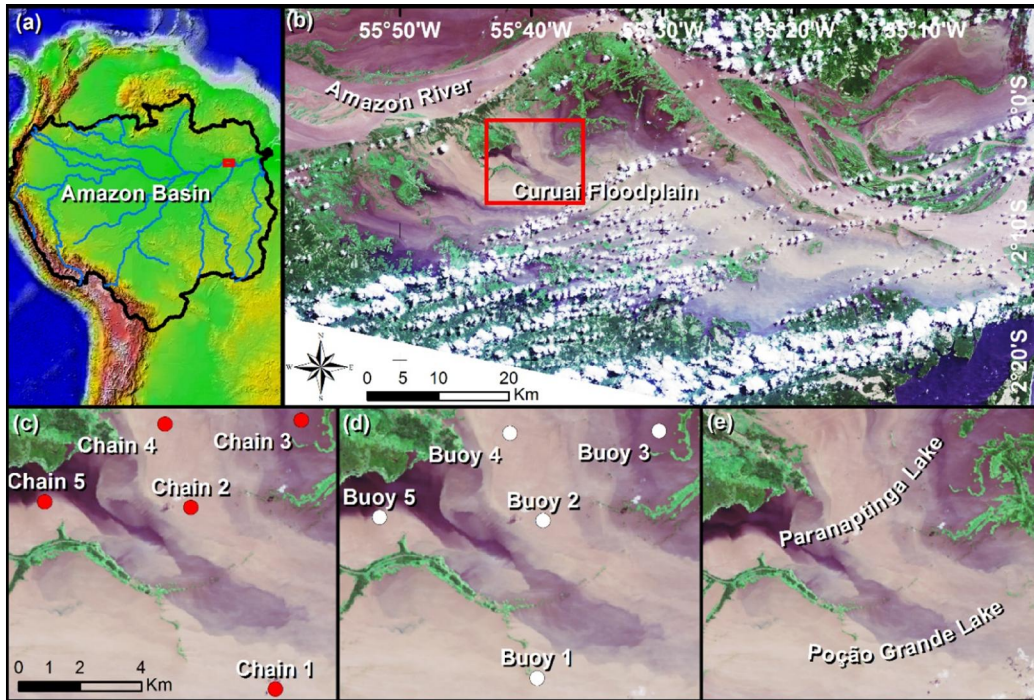
## 2 STUDY SITE

The study was carried out in Lake Paranaatinga (2°4'15.93"S, 55°40'8.03"W) and Lake Poção Grande (2°7'59.47"S, 55°38'52.24"W) located in the northwestern portion of the Curuai flood basin along the southern bank of the lower Amazon River near Óbidos, Pará, Brazil (Figure 2.1). The stage of the Amazon River in this reach varies annually 6 m with a seasonal peak in June and a trough in November. The flooded area of this flood basin ranges from about 850 to 2250 km<sup>2</sup> (RUDORFF et al. 2014a). During low water, sedimentary landforms are exposed and separate the basin into several large, shallow lakes. During high water levels, as was occurring at the time of this study, overbank flow connects the whole flood basin into a complex floodplain lake with flows in the downstream direction sub-parallel to the Amazon River channel (RUDORFF et al., 2014a-b).

Curuai flood basin is a complex of more than 30 large and shallow lakes connected to each other and to the main channel by streams during low water and comprising a floodplain during high water with main flow direction parallel to the Amazon River, with presence of levees and different flooded habitats. The area has been characterized for seasonal variations of water quality (NOVO et al., 2006; FERREIRA et al., 2012; LOBO et al., 2012; SANDER DE CARVALHO et al., 2015; SANDER DE CARVALHO, 2016), flooded environments extent and distribution (ARNESEN et al., 2013) and inundation processes (BONNET et al., 2008; RUDORFF et al., 2014a-b). Advection, wind fetch and solar radiation play significant roles to the mixing patterns of these lakes and the experimental

design was thought to capture the influence of the wind, flow direction and changes in water optical properties.

Figure 2.1: Study site. (a) The Amazon basin and the study site location. (b) True color Landsat 8 composite (date: 07/17/2014) of Curuai floodplain and location of the field measurements. Detail of the distribution of the: (c) thermistor chains; (d) wind buoys and meteorological station (buoy 2); and (e) discrimination of the lakes studied.



The five stations where wind and thermal structure were measured were located along gradients of wind fetch, water depth, flow speed and diffuse light attenuation (Table 2.1, and Figure 2.1). The sampling scheme were thought in order to capture these gradients. Station 1 was located in Lake Poção Grande, while stations 2, 3, 4 and 5 were located in Lake Paranaptinga.

Table 2.1: Lake depth, diffuse light attenuation coefficient ( $K_d$  PAR) and fetch at the field sampling stations. Fetch was measured from east to west on the Landsat 8 image acquired on June 17, 2014. Lake depth and  $K_d$  were measured during the field campaign.

Station	Lake	Depth (m)	$K_d$ PAR ( $m^{-1}$ )	Fetch (km)
<b>1</b>	Poço Grande	7.0	4.3	>20
<b>2</b>	Paranaptinga	6.8	5.0	~4
<b>3</b>	Paranaptinga	5.0	2.6	~2
<b>4</b>	Paranaptinga	4.4	4.9	~5
<b>5</b>	Paranaptinga	4.9	2.3	~9



### 3 FIELD MEASUREMENTS

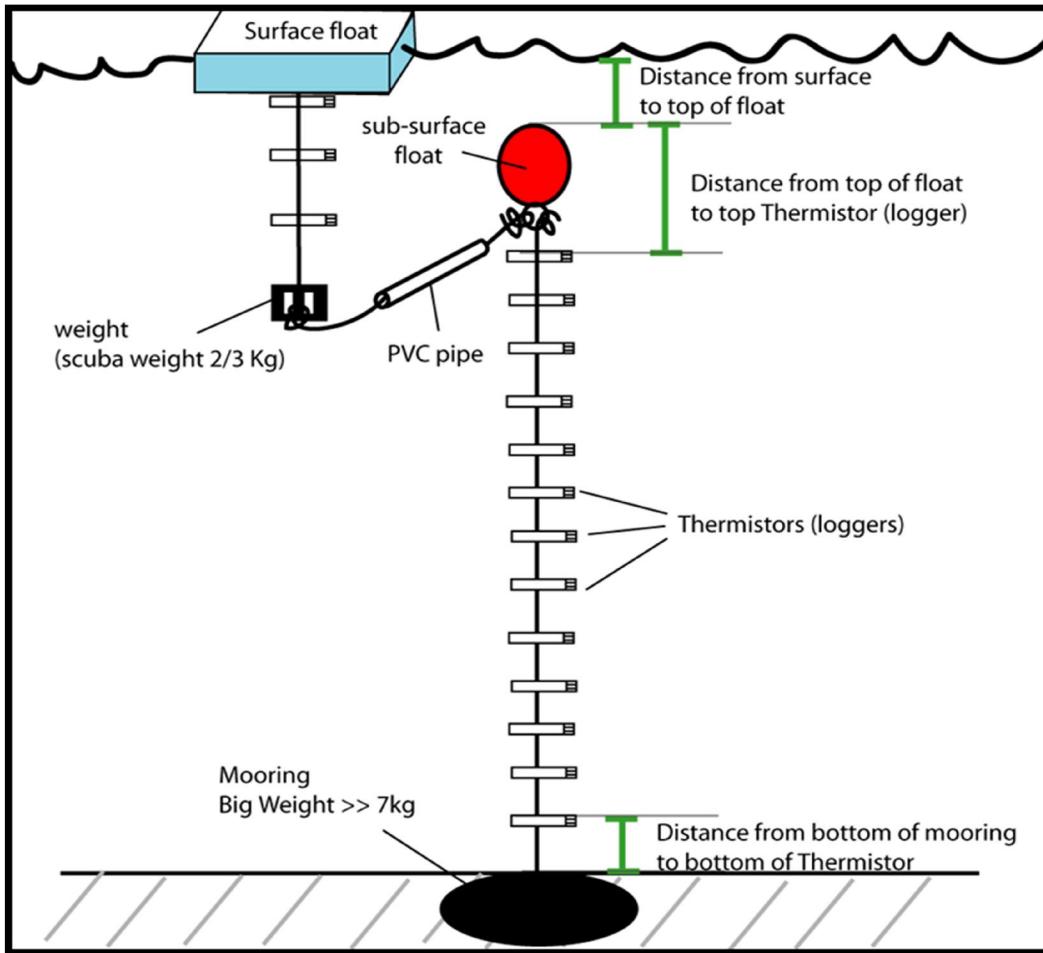
Measurements were made at high water stage from June 23 to July 6, 2014, designated as day 172 to day 186 using day of the year notation. Wind at 2m above the water surface and temperature in the water column were measured at all stations, and station 2 also had sensors to measure solar radiation, air temperature, relative humidity, atmospheric pressure and precipitation. We computed depth averaged current speeds based on hydraulic gradients using the inundation model LISFLOOD-FP. This model was described and applied in the same area by Rudorff et al. (2014, 2018) as a numerical inundation model that offers means to study the interactions among different water sources while accounting for their spatial and temporal variability. It consists in a one-dimensional (1D) simulation of the main channel flood wave and a two-dimensional (2D) simulation of the inundation of the floodplain (Hunter et al., 2007). In LISFLOOD-FP model, channel flow is represented using diffusive or kinematic wave approximations to the full 1D St. Venant equations solved using a fully implicit Newton-Raphson scheme (TRIGG et al., 2009).

Meteorological sensors at station 2 monitored wind speed and direction (HOBO model: S-WCA-M003, manufacturer's specified accuracy  $\pm 0.5 \text{ m s}^{-1}$ ,  $\pm 5$  degrees, resolution  $0.19 \text{ m s}^{-1}$ , and threshold  $0.5 \text{ m s}^{-1}$ ), precipitation (HOBO S-RGB-M002, precision:  $\pm 1.0\%$  up to  $20 \text{ mm h}^{-1}$ ), atmospheric pressure (HOBO S-BPB-CM50, precision:  $\pm 3.0 \text{ mbar}$ ), relative humidity and air temperature (HOBO S-THB-M002, precision:  $\pm 2.5\%$ ,  $\pm 0.2^\circ\text{C}$ ), incoming longwave radiation (Kipp & Zonen CGR 3; sensitivity range:  $5$  to  $15 \mu\text{V/W m}^{-2}$ ), and incoming

shortwave radiation (Kipp & Zonen CMP 3; sensitivity range: 5 to 20  $\mu\text{V/W m}^{-2}$ ). Wind speed was measurable below the reported manufacturer's threshold, and we set the minimum wind speed value to 0.2  $\text{m s}^{-1}$ . Buoys at the other four stations had the same type of wind sensors as station 2. Sampling was at two-second intervals, and data were averaged over 5 minutes.

A thermistor chain was moored at each station. Thermistors (model: U22-001, brand: HOBO, accuracy:  $\pm 0.2^\circ\text{C}$ , resolution:  $0.02^\circ\text{C}$ ) were deployed at 0.02 m (shaded by surface float), 0.5 m and 1.0 m and, thereafter depths were dependent on water depth. The first three loggers were suspended below a surface float on a weighted line and connected to a taut line mooring with a subsurface buoy and anchor on which were attached the other temperature sensors (Figure 3.1). The thermistors had a response time (90% of a step change in temperature) of five minutes, and the sampling times were synchronized. The thermistors sampled every 30 s. All thermistors were inter-calibrated and compared to high resolution sensors in the laboratory (model: RBR solo, accuracy:  $\pm 0.002^\circ\text{C}$ ). Due to the digitization noise associated with the HOBO thermistors, data were smoothed prior to final inter-calibration. In that step, we identified times when the temperature measured by each logger was within  $0.2^\circ\text{C}$  of the others and the water column was assumed to be well mixed. The measured temperature of individual loggers was then shifted such that values were within  $0.02^\circ\text{C}$ .

Figure 3.1: Thermistor chain structure.



Source: MacIntyre (2014).

Spectral measurements of downwelling irradiance ( $E_d$ ) were collected using RAMSES-ACC-UV/VIS (TriOS RAMSES-ACC Oldenburg, Germany – range: 320 to 950 nm, interval: 3.3 nm, accuracy: 0.3 nm). These profiles were collected between 1000 h and 1400 h (local time) at all five sites and were made at approximately 0.1 m intervals in the water column. Depth and inclination measurements were acquired by a pressure and tilt sensor integrated into the radiometer. The radiometric measurements were collected at

a distance of 1.5 meter from the boat, reducing any shading effects. For each sampling point and each depth, ten irradiance measurements were acquired, and the average spectrum was calculated. Calculations were performed for five bands (ultraviolet; 400 to 700 nm - PAR; 700 to 800 nm; 800 to 900 nm; 900 to 1000 nm). Values for bands from 1200 to 1800 nm and 1800-2800 nm were obtained from standard values Jellison and Melack (1993). Attenuation coefficients were calculated using Beer's Law for each wavelength band.

#### **4 STRATIFICATION AND MIXING IN LARGE FLOODPLAIN LAKES ALONG THE LOWER AMAZON RIVER<sup>1</sup>**

Vertical mixing in lakes moderates biogeochemical processes such as resources supply to the upper layers nourishing phytoplankton growth (PATTERSON, 1991), gas exchange at the air-water interface (MACINTYRE et al. 1995, 2010), and development of hypoxia (BOUFFARD et al., 2013) with implications for fish habitat. While temperate and arctic lakes undergo strong seasonal variations in solar radiation and air temperature (MACINTYRE; MELACK, 2009), tropical lakes experience less seasonality in solar radiation and air temperature such that latent heat fluxes and extent of cloud cover are drivers of seasonal and diel variations in stratification (TALLING; LEMOALLE, 1998; MACINTYRE et al., 2002, 2014). With warm surface temperatures, evaporation rates can be higher in tropical lakes for the same wind speed causing deeper mixing when solar radiation is reduced than in more northerly lakes (MACINTYRE; MELACK 2009). Consequently, shallow tropical lakes typically undergo diel cycles of stratification and mixing (TALLING, 1969; GANF, 1974; MELACK; KILHAM, 1974). Additional variability caused by changes in water level, connectivity to rivers and optical properties are likely for floodplain lakes.

---

<sup>1</sup> This chapter is based on the published paper: Stratification and mixing in large floodplain lakes along the lower Amazon River, by Pétala Bianchi Augusto-Silva, Sally MacIntyre, Conrado de Moraes Rudorff, Alicia Cortés, John Michael Melack, published in the Journal of Great Lakes Research, Volume 45, Issue 1, 2019, Pages 61-72, ISSN 0380-1330, <https://doi.org/10.1016/j.jglr.2018.11.001>.

The diel cycles of stratification and mixing within floodplain lakes are expected to be influenced by the surface energy budget, as in other lakes, and wind as it induces up and downwelling of diurnal thermoclines and causes horizontal transport. Horizontal advection from riverine inflows; differences in lake morphology; changes in light attenuation that are moderated by the inflows due to sediment deposition and the passage of the water through vegetated environments that alters its compositions; can also be sources of variability. Aquatic vegetation will contribute by moderating the light climate and water velocities. For example, in the lowlands of large tropical rivers, seasonal floods cause variations in water level, flow, sediment concentration and extent of aquatic vegetation on the fringing floodplains (MELACK et al., 2009).

Prior work in the central Amazon basin has shown the depth dependence of vertical mixing. When lakes are less than about 4 m deep, they tend to be vertically mixed at sunrise, develop a diurnal thermocline towards midday under low winds, and mix again at night (MELACK; FISHER, 1983; TUNDISI et al., 1984; MACINTYRE; MELACK, 1984, 1988). As lakes exceed 6 m in depth, seasonal stratification develops and often persists for days to weeks with diel variations in the depth of the upper mixing layer (MACINTYRE; MELACK, 1988; ENGLE; MELACK, 2000; CARABALLO et al., 2014). The extent to which they are influenced by horizontal advection from riverine inflows, wind, differences in lake morphometry, aquatic vegetation and sediment load, as it moderates changes in light attenuation are unknown, particularly for the larger floodplain lakes of lowland Amazon floodplain.

Changes in floodplain hydrology, channel gradient, lake sizes, bathymetry and sediment transport which occur along the Amazon River valley should lead to differences in mixing within the lakes (SIPPEL et al., 1992; MERTES et al., 1995; DUNNE et al., 1998). For instance, for the ria lakes in the central Amazon where earlier studies were conducted, rainfall and local runoff were found to be larger components of the water budget than incoming riverine flows (LESACK; MELACK, 1995). In contrast, in the eastern basin, sediment-laden riverine inputs represents a large fraction of the incoming water (RUDORFF et al., 2014b). For this region, the rate of lateral migration of the main channel is lower than upstream, and floodplain construction is dominated by overbank deposition, which formed large, shallow lakes surrounded by sedimentary landforms (SIPPEL et al., 1992; MERTES et al., 1995; DUNNE; AALTO, 2013).

During high water, the shallow regions between the river and lake may heat and cool faster than deeper locations farther from the banks and, with ongoing overbank flow, moderate thermal structure for some distance downstream. Vegetation in shallow areas may cause the flows to lose momentum and deposit particulates, such that the waters become clearer.

Given the abundance and ecological significance of these large, shallow, tropical, floodplain lakes in the lowland Amazon basin, and similar floodplain regions elsewhere in the tropics, the following questions were addressed in the aim to understand the vertical mixing dynamics of this class of lakes: (i) how does the thermal structure and extent of vertical mixing vary spatially within the lakes?; and (ii) what physical processes control the vertical thermal structure?

Despite the basic understanding of the importance of diel stratification and mixing, surface energy budgets, including the quantification of turbulent velocity scales, and advection over kilometer scales have rarely been computed for tropical lakes. A multi-station measurements set was built to provide new data and understanding of spatial differences in stratification and mixing and controls on between station variability.

Time series measurements of surface meteorology and water column thermal structure were acquired together with measurements of light attenuation and water currents. With these measurements, spatial and temporal changes in thermal structure were characterized and shifts in dominance of production of turbulence between wind and convective cooling were examined at diel timescales. Also, the calculated surface heat budget was contrasted with the measured heat content to assess whether advection was moderating the extent of heating and the thermal structure. This study has implications for the representation of shallow tropical lakes in land surface models (DADSON et al. 2010; RILEY et al. 2011; SUBIN et al. 2012) and improved estimates of trace gases exchange with the atmosphere (RUDORFF et al. 2011; MELACK, 2016).

## **4.1 Methods**

### **4.1.1 Surface energy budget, turbulent velocity scales, and heat budgets**

The estimates made in this section followed Imberger (1985) and MacIntyre et al. (2002, 2014). Sensible heat (SE) is the heat that leads to changes in the temperature of a given body, and latent heat fluxes (LE) is the heat that is used to change the physical state of given body without changing its temperature.

Both heats were estimated using the aerodynamic formulas  $SE = \rho_A C_{Pa} C_H U_Z (T_S - T_Z)$ , and  $LE = \rho_A L_V C_E U_Z (q_S - q_Z)$ , where:  $\rho_A$  is the density of the air at the air-water interface;  $U_Z$  is the wind speed at height  $z$  above the water surface;  $SE$  is the sensible heat transfer;  $C_{Pa}$  is the specific heat of air;  $C_H$  is sensible heat transfer coefficient;  $T_S$  is the water surface temperature;  $T_Z$  is the air temperature at height  $z$ ;  $LE$  is the latent heat transfer;  $L_V$  is the latent heat of vaporization;  $C_E$  is latent heat transfer coefficient;  $q_S$  is the specific humidity at saturation pressure at  $T_S$ ; and  $q_Z$  is the specific humidity of the air at  $z$ .

The measurements of  $U_Z$ ,  $T_Z$  and relative humidity (RH) were taken ~2 m above the water surface. The neutral values of the transfer coefficients at 10 m height ( $C_{DN}$ ,  $C_{HN}$  and  $C_{EN}$ ) were adjusted for the measurement height following the method of Amorocho and DeVries (1980). These coefficients were corrected for atmospheric stability following the iterative approach suggested by Hicks (1975) and using the method of Monin and Obukhov (1954) based of the length of Monin-Obukhov ( $L$ ).

The outgoing longwave radiation ( $LW_{out}$ ) is the energy radiating from the a given body as infrared radiation. It was calculated as  $LW_{out} = \epsilon_w \sigma T_S^4$ , where:  $\epsilon_w$  is the emissivity of water ( $0.97 \pm 0.005$  - Anderson, 1954) and  $\sigma$  is the Stefan-Boltzman constant ( $5.67 \times 10^{-8} W \times K^{-4} \times m^{-2}$ ). The surface heat flux, which is the energy balance of a surface layer, was computed as the sum of latent heat flux, sensible heat flux and net long wave radiation ( $LW_{net}$ ), which is the result of the longwave radiation that is reaching a given body ( $LW_{in}$ ) less the longwave

radiation emitted by this body ( $LW_{out}$ ), i.e.  $LW_{net} = LW_{in} - LW_{out}$ . The effective heat flux ( $H^*$ ) for the actively mixing layer is the sum of the surface heat flux plus the shortwave radiation retained within the actively mixing layer.

Buoyancy flux ( $B$ ) is defined as the vertical kinematic flux of a virtual potential temperature. This parameter was computed from the effective heat flux (IMBERGER, 1985):

$$B = \frac{g\alpha H^*}{C_{Pw}\rho_0}$$

where:  $g$  is the acceleration due to gravity;  $\alpha$  is the thermal expansion coefficient as a function of the temperature;  $\rho_0$  is freshwater density; and  $C_{Pw}$  is the specific heat of water.

Near surface turbulence is caused by wind and cooling. The water friction velocity ( $u_{*w}$ ) provides an index of the contribution from wind and is computed from shear stress,  $\tau = \rho_A C_D U_Z^2 = \rho_A u_*^2 = \rho_W u_{*w}^2$  based on the assumption that surface shear stress is the same on both sides of the air-water interface. Here  $\rho_A$  and  $\rho_W$  are the density of the air and water, respectively ( $kg\ m^{-3}$ );  $U_Z$  is the wind speed at height  $z$  above the water surface ( $m\ s^{-1}$ ); and  $C_D$  is the drag coefficient at measurement height corrected for atmospheric stability. The penetrative convection velocity ( $w_*$ ), indicates the velocity of thermals due to cooling. It is computed as  $w_* = (Bh)^{1/3}$  where  $h$  is the depth of the actively mixing layer (DEARDOFF, 1970; IMBERGER, 1985). Total turbulent energy flux into the surface layer,  $F_q$ , is calculated as  $F_q = 0.5(w_*^3 + C_N^3 \cdot u_{*w}^3)$ , where  $C_N$  is a

coefficient equal to 1.33. This value represents the energy introduced in the water by both shear production and surface cooling (KIM, 1976; RAYNER, 1981; IMBERGER, 1985).

#### 4.1.2 Length of Monin-Obukhov ( $L_{mo}$ )

The ratio of the convection term to the total production of turbulent kinetic energy (TKE) term was computed to determine when convection dominated TKE production. This ratio is known as the Monin-Obukhov length scale ( $L_{mo}$ ) and it represents the depth at which the production of TKE due to wind shear equals the production of TKE due to buoyance forces. In the water this length is:

$$W = \frac{(g / \rho) \Delta \rho h^2}{u_{*w}^2 L}$$

where  $u_{*w}$  is the shear velocity equals to the root of the shear stress due to wind divided by the water density ( $\sqrt{\tau / \rho_w}$ ) and B is the buoyance flux. If B is positive,  $L_{MO}$  is called  $L_{MO}$  heat, if B is negative,  $L_{MO}$  is called  $L_{MO}$  cool. Above the depth equal to the absolute value of the  $L_{MO}$ , wind shear is assumed to dominate the production of TKE. Below that depth, the turbulence is assumed to be suppressed when the water column is warming (stabilizing) and enhanced when the water is cooling (destabilizing).

### 4.1.3 Stratification and the depth of the actively mixing layer

Due to the accuracy of the temperature loggers, the depth of the actively mixing layer (h) was computed as the depth where temperature was 0.02°C lower than that at the surface. In addition, when the temperature difference between the two uppermost loggers (0.02 m and 0.5 m) was larger than 0.02°C, the depth of the shallow actively mixed layer was defined to be midway between them, i.e. 0.24 m.

Stratification was quantified as the buoyancy frequency,  $N = [(g/\rho) dp/dz]^{1/2} \cdot 3600/2\pi$ . It is the frequency at which a vertically displaced water parcel will oscillate. The parcel, which is vertically perturbed from its initial position, experiences a vertical acceleration. If the acceleration is towards the original position, it is a case of stable stratification and  $N^2 > 0$ . If the acceleration is away from the original position and  $N^2$  is less than zero, the stratification is unstable.

Wedderburn number (W) was calculated as:

$$W = \frac{(g/\rho)\Delta\rho h^2}{u_{*W}^2 L}$$

where  $\Delta\rho$  is the density difference across the diurnal thermocline and L is the fetch (IMBERGER, 1985). This number is a parameter used to measure the balance between wind and buoyancy force and it is normally used to infer the occurrence of upwelling. The magnitude of downwelling increases as W decreases, with partial downwelling even with  $W=12$  (MONISMITH, 1986).

Fetch for station 2 was fixed at 4 km and, with large fetches at all stations, interpretation for  $W$  will remain the same even if  $L$  varies.

#### **4.1.4 Advection**

Advection as the transport by bulk motion was inferred by comparing the heat fluxes in the lake computed from the surface energy budget using meteorology data ( $Q_M$ ) and from the time series temperature measurements ( $Q_T$ ).  $Q_T$  was computed as the sum of the change of heat content in the individual layers  $Q_T = \rho_w \cdot C_{p_w} \cdot \Delta T(\Delta t, \Delta z) \cdot \Delta z$ , where  $\rho_w$  is water density,  $C_{p_w}$  is the specific heat of water,  $\Delta T$  is the mean temperature integrated in time ( $\Delta t$ ) and depth ( $\Delta z$ ) where  $\Delta T$  is two hours and delta  $z$  was the depth between loggers. If  $Q_M$  and  $Q_T$  are equal, then there is no bulk motion and the heat content in the water column can be estimated based on meteorology only. However, if they diverge, then there must be bulk motion involved.

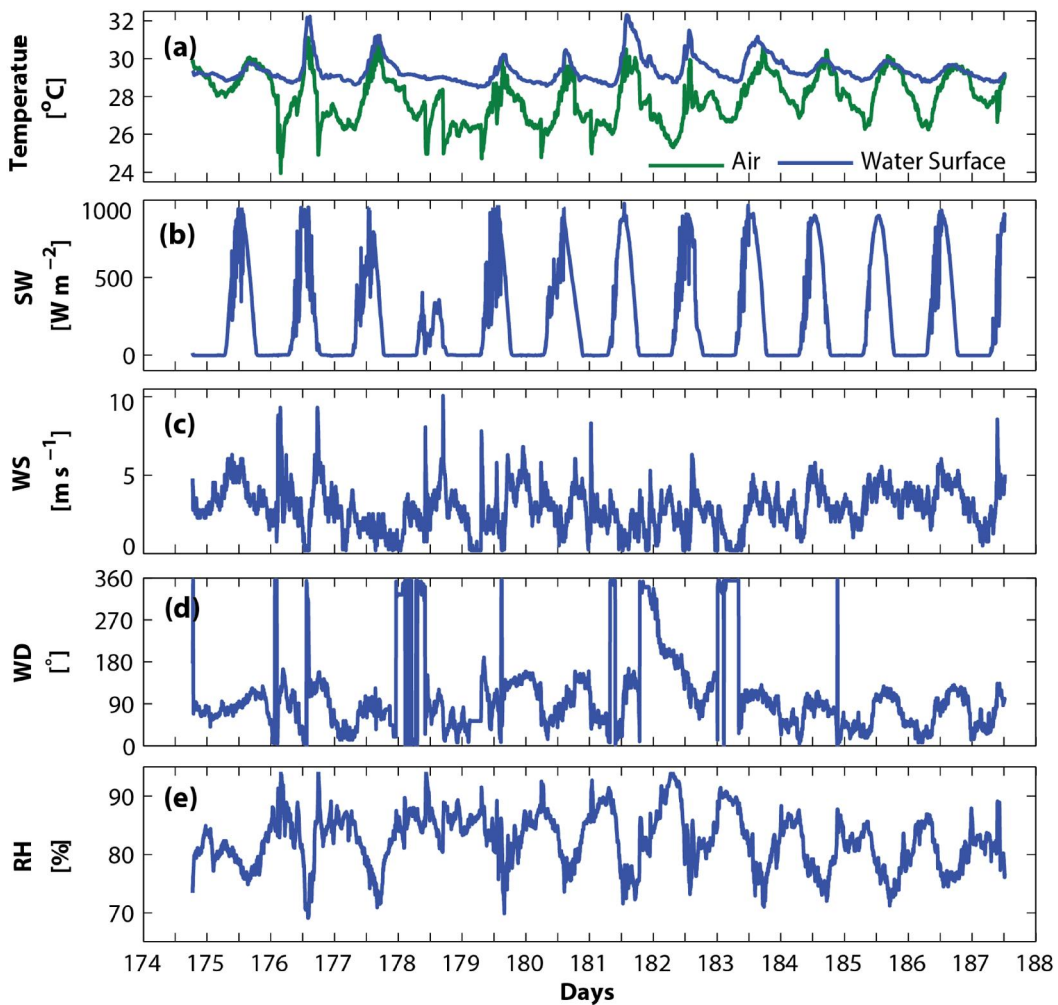
## **4.2 Results**

### **4.2.1 Meteorology**

The measurement acquisition can be divided into two periods according to differences in weather. The first period, prior to day 181, had cooler nights, greater cloud cover and a tendency for wind to drop below  $1 \text{ m}\cdot\text{s}^{-1}$  around midday and at night (Figure 4.1). Relative humidity at night was lower in the second period with reduced cloud cover, and a pattern of low winds at night from the north and stronger winds in the afternoon from the east was more

consistent. In the first period, the nights were 3°C cooler than surface waters and in the second, 2°C colder. Peak wind speed was ~5 m.s<sup>-1</sup> for both periods. Winds more frequently dropped to the instrument threshold at night during the first period. Day 178 differed from the others in that it was overcast with high relative humidity, low shortwave radiation, and showers of 12.4 mm of rainfall in the morning and 2.2 mm in the afternoon (data not shown). Winds reached 10 m s<sup>-1</sup> during rainstorms.

Figure 4.1: Five-minute averages of meteorological data from station 2: (a) air temperature and near-surface water temperature; (b) shortwave incoming radiation (SW); (c) wind speed (WS); (d) wind direction (WD); and (e) relative humidity (RH).



Air temperature ranged from 23.9°C around midnight to 31.1°C around 13:00 (local time) and had an overall mean of 27.9°C (Figure 4.1a). Surface water temperature tended to be warmer than air temperature except for a few hours in the afternoon for about half the days (Figure 4.1a). Consequently, the atmosphere above the lake usually was neutral or unstably stratified. Shortwave radiation reached  $1000 \text{ W m}^{-2}$  at noon under clear sky conditions and varied rapidly in response to changes in cloud cover (Figure 4.1b). Relative humidity was lowest at midday (minimum of 69%) and peaked around midnight (maximum of 95%) with a mean of 82% (Figure 4.1e).

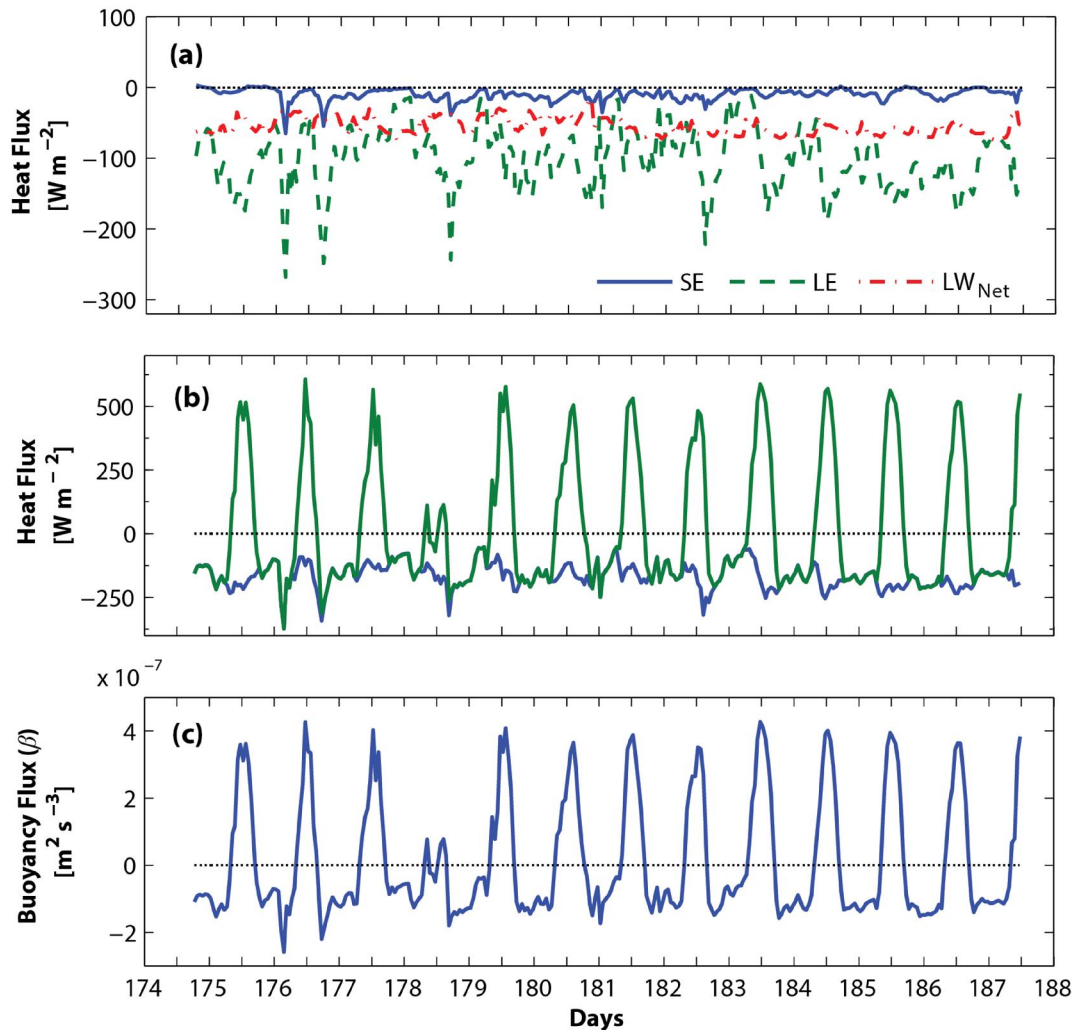
Heat losses from evaporation, that is, latent heat fluxes, exceeded the other loss terms in the surface energy budget (Figure 4.2a). As wind speed increased, latent heat fluxes increased from  $\sim -50$  to  $\sim -150 \text{ W m}^{-2}$ , reaching up to  $-400 \text{ W m}^{-2}$  in response to squalls. Sensible heat flux was the smallest term in the surface energy budget with values close to  $0 \text{ W m}^{-2}$  except during the squalls when SE losses reached  $\sim -100 \text{ W m}^{-2}$ . Net longwave radiation averaged  $-50 \text{ W m}^{-2}$  during the initial cloudier period and  $-100 \text{ W m}^{-2}$  for the second period with its clearer skies.

The surface heat flux had values generally between  $-100 \text{ W m}^{-2}$  and  $-200 \text{ W m}^{-2}$  (Figure 4.2b). As a result of high solar radiation and these relatively low surface heat fluxes, due to predominantly light winds and modest latent heat fluxes except during squalls, the effective heat flux was high and became positive only about an hour after sunrise and negative in the afternoon approximately an hour before sunset (Figure 4.2b). Maximum daily values reached  $600 \text{ W m}^{-2}$ . On day 178, the effective heat flux was negative in the day due to persistent cloud

cover. Positive values of the buoyancy flux followed the same pattern as shortwave radiation, and values were negative at night and  $\sim -1 \times 10^{-7} \text{ m}^2 \cdot \text{s}^{-3}$  (Figure 4.2c).

As in Pilkington Bay (MACINTYRE et al., 2002), in these lakes of Curuai floodplain, evaporation was the main cause of heat loss (Figure 4.2a), therefore wind contributes to surface layer deepening by inducing both turbulence in the water column and heat loss at the air-water interface. Wind is also responsible for tilting the thermocline in the main wind direction (east to west or from chain 3, to chain 2 and then chain 5), which is likely the reason why upwelling of colder water can be observed at some stations.

Figure 4.2: (a) Hourly time series of components of the surface energy budget: sensible heat flux (SE), latent heat flux (LE), and net longwave radiation ( $LW_{Net}$ ); (b) Surface heat flux (blue line) and effective heat flux (green line) into the actively mixing layer; and (c) Buoyancy flux.



#### 4.2.2 Turbulent velocity scales

The magnitude of non-zero values of  $u_{*W}$  and  $w_*$  ranged from  $0.1 \text{ cm s}^{-1}$  during light winds to  $1 \text{ cm s}^{-1}$  with the highest values during squalls (Figure 4.3a). Water friction velocity,  $u_{*W}$  peaked midday to early afternoon with typically lower values at night and through midmorning of the next day. The timing of its

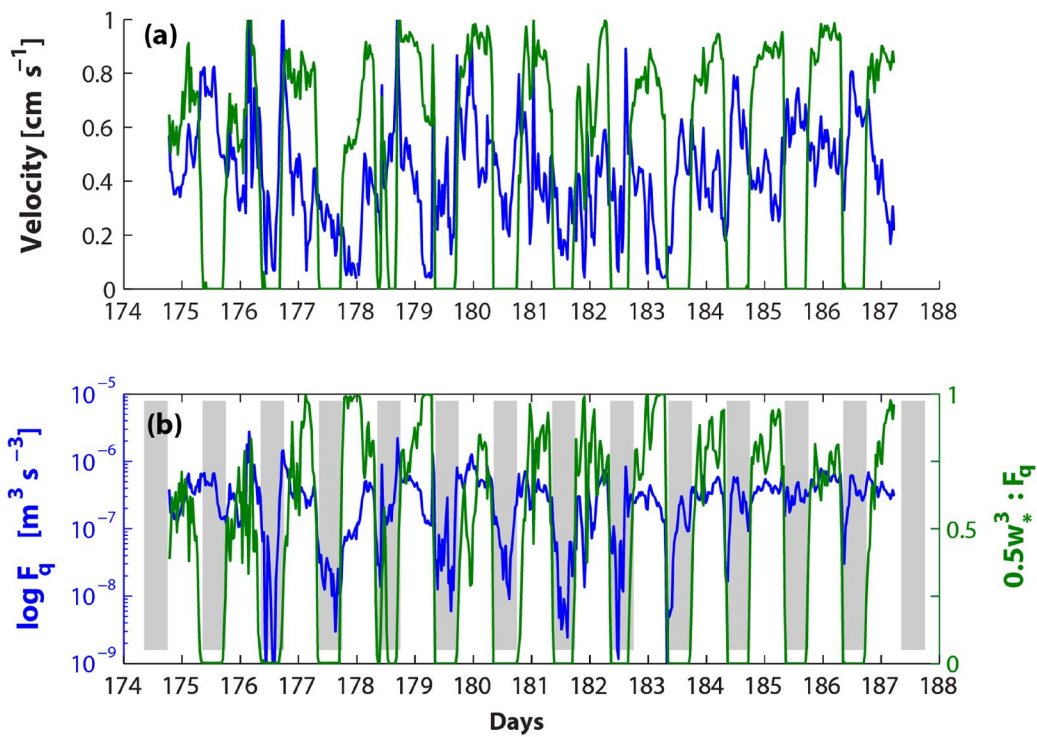
maximum varied between the first (prior to day 181) and second period of our study. For much of first period, values were low during heating and reached a maximum with the transition to cooling. Values were about half during heating in the first period compared to the second period, where they were maximal. Thus, shallow diurnal thermoclines are expected during heating for much of the first period and deeper ones during the second with the accompanying wind induced mixing.

Penetrative convection velocity,  $w_*$  was zero in the day when  $B$  was positive and approached  $1 \text{ cm s}^{-1}$  at night. With the later onset of higher winds during the first period, both  $u_{*W}$  and  $w_*$  were elevated as cooling began, however winds often decreased at night such that convection subsequently dominated. For both periods,  $w_* > u_{*W}$  for much of the night.

$F_q$  varied over several orders of magnitude (Figure 4.3b). Half hour averages ranged from  $10^{-9} \text{ m}^3 \text{ s}^{-3}$  to  $10^{-8} \text{ m}^3 \text{ s}^{-3}$  during morning heating with negligible winds and exceeded  $10^{-7} \text{ m}^3 \text{ s}^{-3}$  under heating and moderate winds. Values at night also ranged from  $10^{-7} \text{ m}^3 \text{ s}^{-3}$  to  $10^{-6} \text{ m}^3 \text{ s}^{-3}$  except during brief windy periods when they exceeded  $10^{-6} \text{ m}^3 \text{ s}^{-3}$ . On the few occasions when winds dropped at night,  $F_q$  decreased by an order of magnitude. Hourly averages of the ratio  $0.5w_*^3 : F_q$ , which applies during cooling, generally had values in excess of 0.7, indicating the strong contribution of cooling to turbulence production. The low values of  $F_q$  during morning heating with low wind enables the development of strong stratification which is disrupted by persistent cooling at night. With current speed at all sites reaching  $0.1 \text{ m s}^{-1}$  (measurements made at each site

using a SonTek/YSI Inc. 1.5 MHz Acoustic Doppler Current Profiler – ADCP), some turbulence may have been induced by shear from advection. However, we have insufficient current measurements to quantify the contribution from that source.

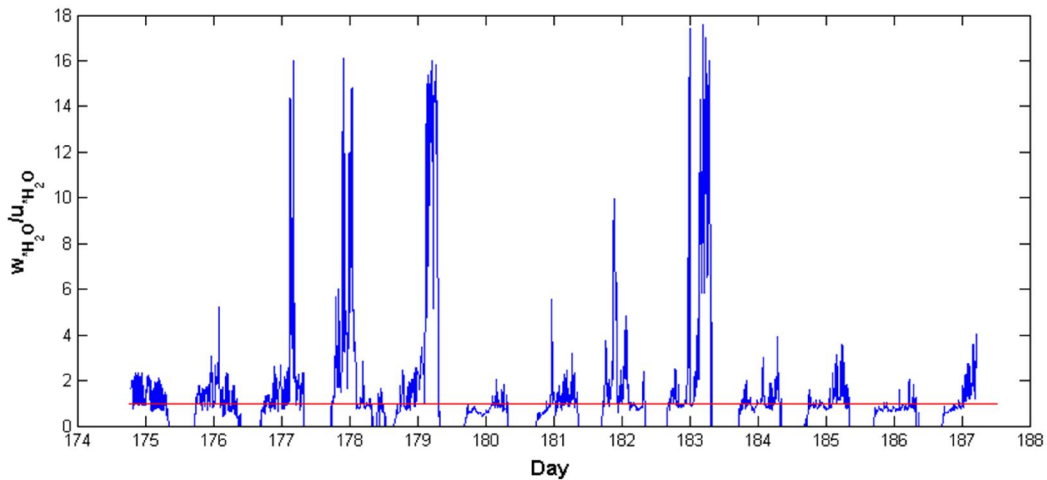
Figure 4.3: (a) Water friction ( $u_{*W}$ , blue line) and penetrative convection velocity ( $w_*$ , green line); and (b) Half hour averaged turbulent energy flux into the actively mixing layer ( $F_q$ ) (blue, left axis) and the ratio  $0.5w_*^3:F_q$  (green, right axis). Computed for station 2 except on days 174 to late afternoon on day 177 when the gaps were filled using computations from Station 1.



The lakes studied stratified to the surface at midday when  $F_q$  was least, i.e., when there was no cooling and the wind was low. Following the pattern observed in Pilkington Bay by MacIntyre et al (2002), the surface layer deepened as  $F_q$  increased, and, since this parameter is dependent on  $w_{*W}$  and  $u_{*W}$ , examination of the ratio between these two individual terms (Figure 4.4)

allows assessment of the contribution of wind forcing and cooling to the surface layer deepening at different times of day. A ratio equal to one (red line) would represent equal contribution of cooling and wind. If the ratio is more than one, the larger contribution is due to cooling; if the ratio is lesser than one, the larger contribution is due to wind stirring. At station 2, surface layer deepening was dominated by convective cooling during the night and by wind stirring during the day (Figure 4.4). The only exception to that was day 178, which was an overcast day.

Figure 4.4: Ratio between penetrative convection velocity and water shear velocity. Red line represents ratio equals to one.



The ratio  $0.5w_*^3 : F_q$  (Figure 4.3) represents the ratio of the buoyancy flux to total kinetic energy flux. In all stations this ratio was zero during the day, which indicates that turbulence generate during this period was not driven by density but by wind. We plotted the histograms of this ratio in the water column with 1 m depth intervals (data not shown). The result of this analysis is summarized in Table 4.1 and shows that the extent of the influence of wind stirring in the water

column varies among the stations. At stations 3 and 4 data were not sufficient for computing the equilibrium between wind stirring and convective cooling contribution to the depth of the surface layer.

Table 4.1: Result of the histograms of the ratio  $0.5w_*^3 : F_q$  in all stations.

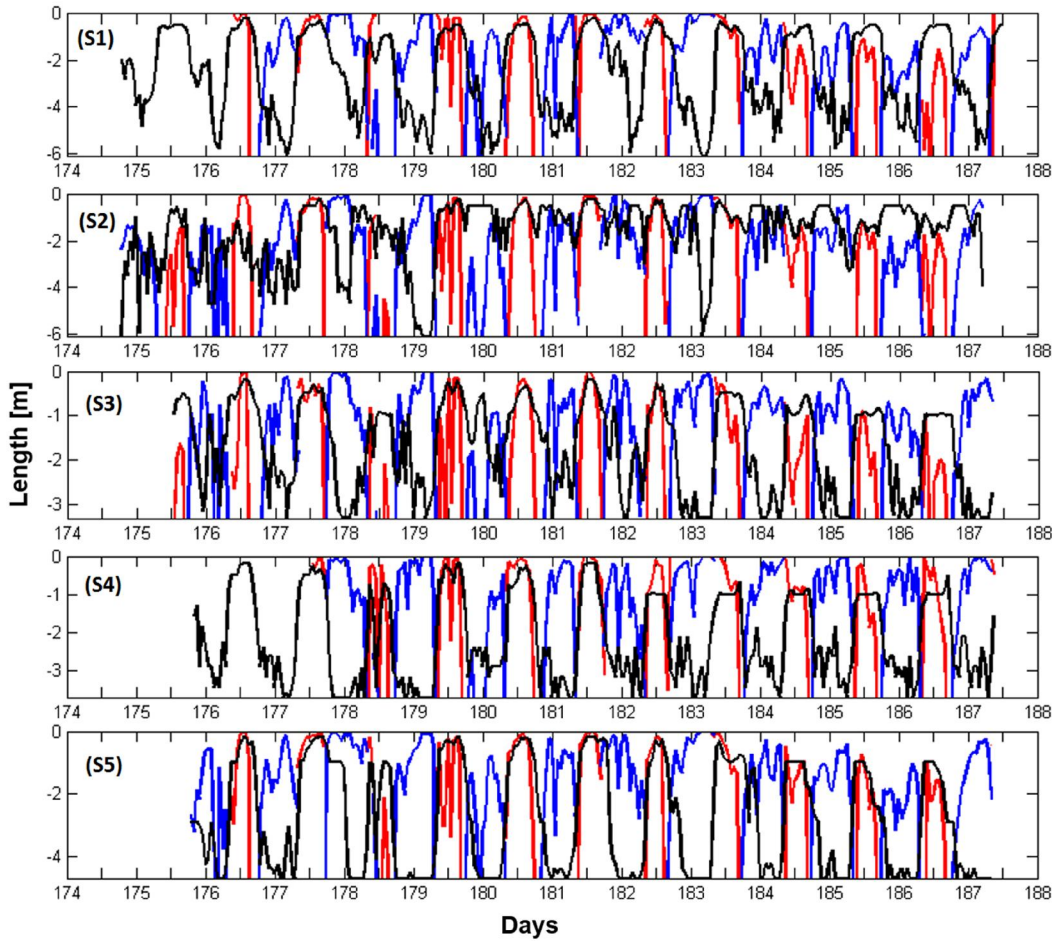
Station	Wind domain	Equilibrium	Convection domain
1	$\leq 1\text{m}$	$>1\text{m and } \leq 2\text{m}$	$> 2\text{m}$
2	$\leq 3\text{m}$	$>3\text{m and } \leq 4\text{m}$	$> 4\text{m}$
3	$\leq 1\text{m}$		$> 2\text{m}$
4	$\leq 3\text{m}$		$> 3\text{m}$
5	$\leq 2\text{m}$	$>2\text{m and } \leq 3\text{m}$	$> 3\text{m}$

The results shown in Figures 4.3 and 4.4 demonstrate that surface layer deepening was dominated by wind stirring during the day, and the results from Table 2 indicates that wind contribution is limited to a certain depth, which is variable among the stations analyzed.

#### 4.2.3 The Length of Monin-Obukhov ( $L_{MO}$ ) in the water and the actively mixing layer (h)

Figure 4.5 shows a comparison of  $L_{MO}$  and h for all stations during the experiment. From the analysis of this figure we can see two separate patterns: a nocturnal one and a diurnal one, both described below.

Figure 4.5:  $L_{MO}$  in the water (cool in blue, heat in red) and  $h$  (black line) with subpanels ordered from station 1 (S1) to station 5 (S5).



#### 4.2.3.1 Nocturnal pattern

$L_{MO}$  is shallower than  $h$  in all stations every night. This divides the surface mixing layer in an upper thin part where wind shear dominates the production of TKE and a lower deeper region where the production of TKE is dominated by buoyancy forces, i.e. convective cooling. When the buoyancy flux is negative ( $L_{MO-cool}$ ) the water column is destabilizing. As the mixing depth ( $h$ ) reaches the bottom every night for all stations and the  $L_{MO}$  is shallow, negative buoyancy fluxes dominate the production of TKE during the night.

#### **4.2.3.2 Diurnal pattern**

At daybreak,  $L_{MO}$  shifts from cooling to heating and the water column begins to stabilize and reduce  $h$  with warming from solar radiation at the surface. Both  $h$  or the  $L_{MO}$  are shallow and have small difference in depth. This demonstrates that the wind contribution to the production of TKE is restrict to this thin superficial layer, i.e. wind shear is not capable of breaking the stability of the water column due to high insolation. Wind contribution to the production of TKE only rises in depth at the beginning and at the end of the sun light availability.

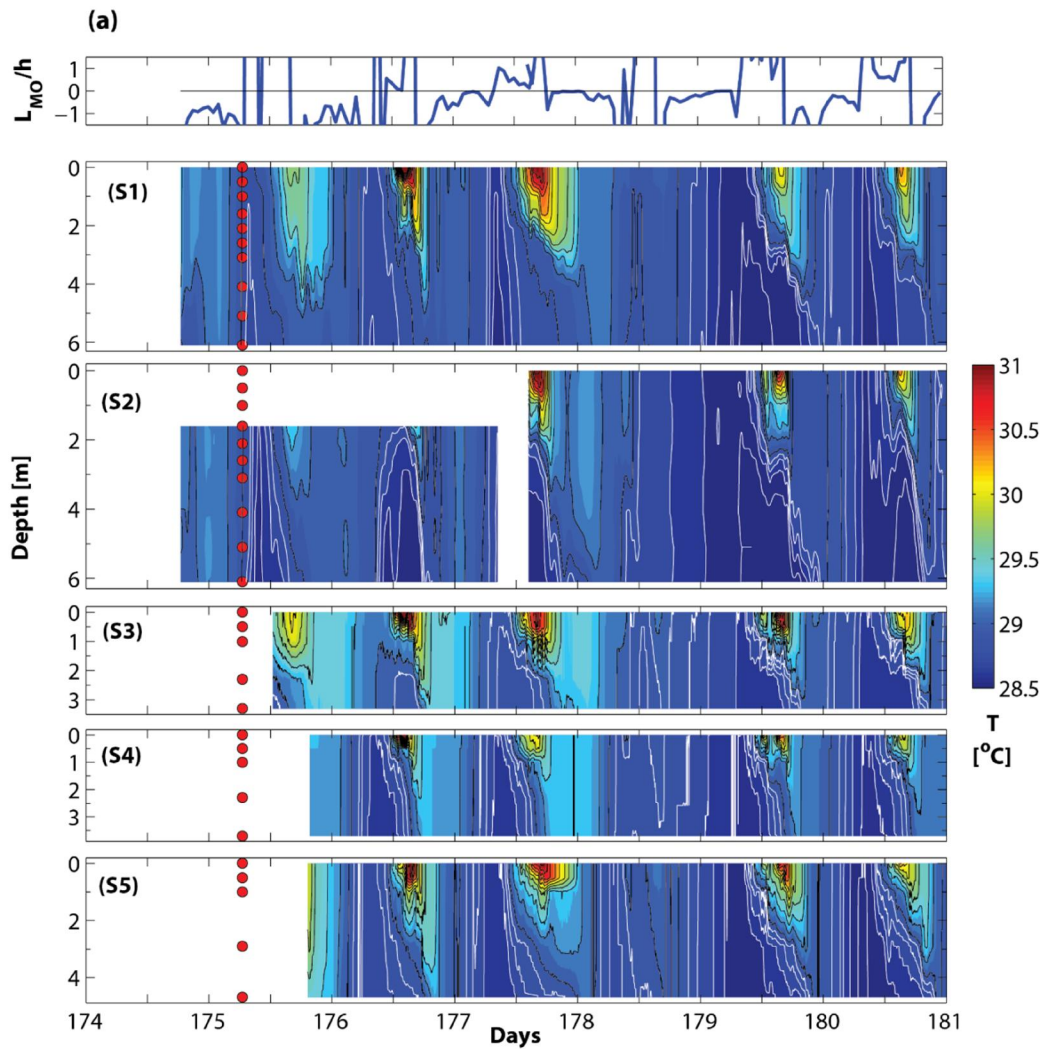
During day 178, the water column begins its superficial warming period, but due to rain and less solar radiation, there are many oscillations from  $L_{MO}$ -heat to  $L_{MO}$ -cool. A shallow  $h$  is stablished during this day, but not as shallow and stable as the other days.  $h$  was shallower than the  $L_{MO}$ , meaning that the production of TKE in the surface mixing layer is dominated by wind shear with tendency to deepening due to shifts from  $L_{MO}$ -heat to  $L_{MO}$ -cool, leading to complete mixing of the water column in all stations.

#### **4.2.4 Thermal stratification**

The diffuse attenuation coefficient,  $K_d$ , was high ( $2-5 \text{ m}^{-1}$ ) at all sites (Table 2.2).  $K_d$  was highest at stations 2 and 4 along a turbid plume of incoming river water, slightly lower at station 1 located further into the floodplain, in Lake Poção Grande, and lowest at the sites where river water flowed through vegetation (station 3 and 5). As expected with these high values of  $K_d$ , shallow diurnal thermocline formed at all sites under morning heating with light winds

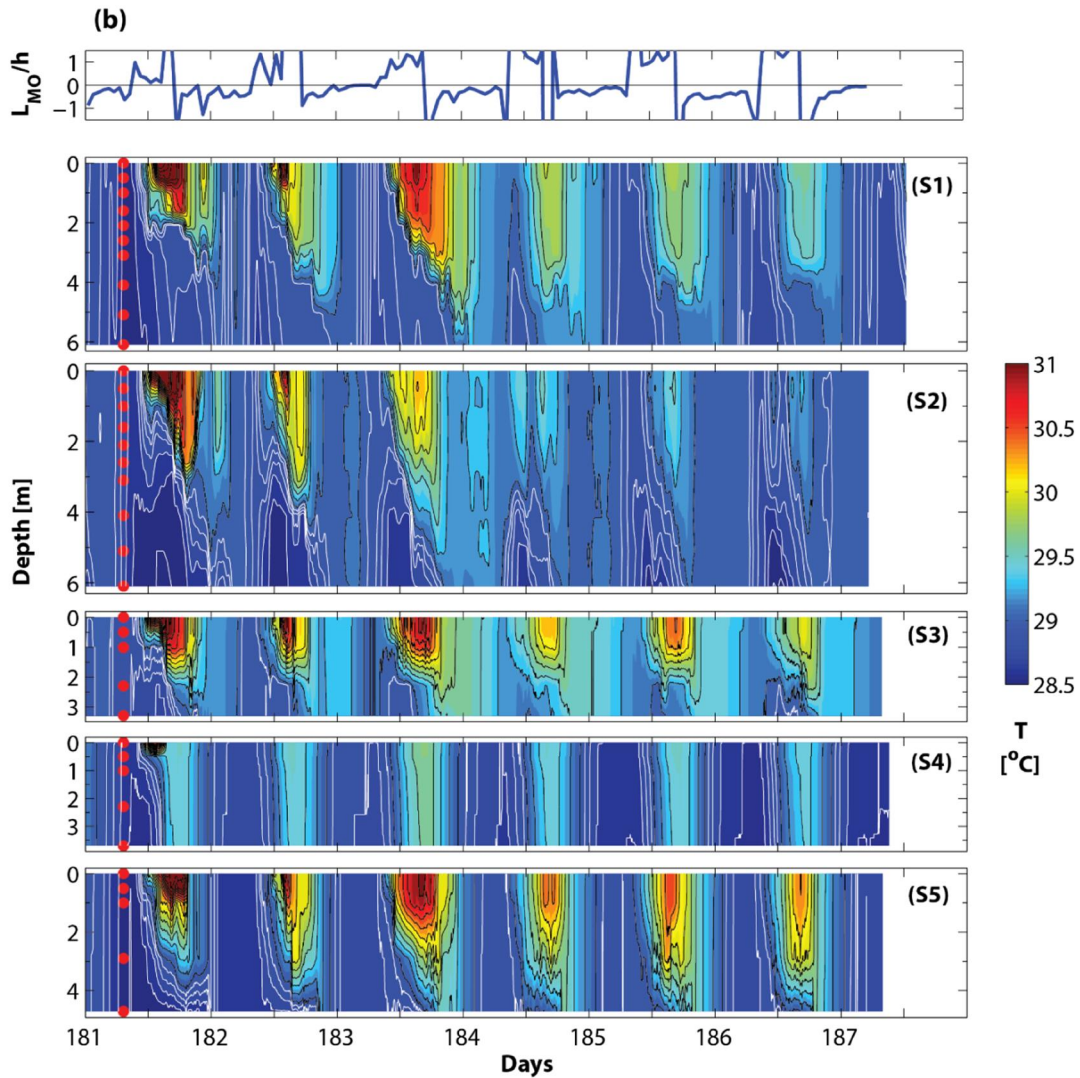
Comparison of time-depth diagrams of water temperature shows the overall pattern is one of diurnal heating and nocturnal cooling with mixing at night reaching to the bottom at each site (Figure 4.6). Variability was induced by proximity to the incoming river water and exposure to wind.

Figure 4.6: Top panel: Hourly averages of  $L_{MO}/h$  for station 1, first three days, and station 2 thereafter, and lower panels: Time-depth diagrams of water temperature for: (a) days 174-180 and (b) days 181-187. Subpanels are ordered from station 1 to station 5. Isotherms are every  $0.1^{\circ}\text{C}$  below  $29^{\circ}\text{C}$  (white) and every  $0.2^{\circ}\text{C}$  above that temperature (black). Positive values of  $L_{MO}/h$  indicate heating, and the ratio equals fraction of the actively mixing layer mixed by wind. Red dots indicate the thermistor positions for each chain. Upper three thermistors on chain 2 were lost after initial deployment and replaced on day 178.



continue

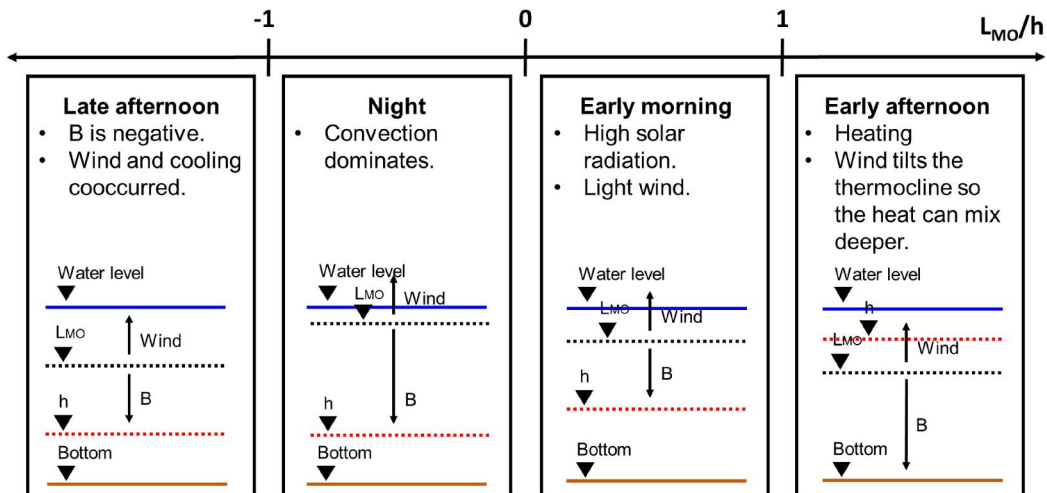
Figure 4.6: Conclusion.



Near-surface temperatures and stratification were higher when  $0 < L_{MO}/h < 1$ . As the sign of  $L_{MO}/h$  became positive, indicating heating, temperature began to increase. In most cases,  $L_{MO}/h$  approached 1 at the onset of heating, implying, as observed, that heat would be mixed throughout the actively mixing layer. Shortly thereafter on a few of the days,  $L_{MO}/h$  approached zero. Stratification reached the surface and the base of the diurnal thermocline was at  $\sim 1$  m. The high near-surface temperature and strong near surface stratification that

resulted is particularly notable on days 176, 177, 181, and 182. When  $L_{MO}/h$  increased again in the afternoon to values near 1 with the onset of intensified winds, the diurnal thermocline downwelled. In the second half of the study,  $L_{MO}/h$  remained near 1 or higher midday. The increased mixing led to cooler near-surface temperature and weaker near surface stratification than in the first half of the study. The onset of cooling was typically associated with increased winds, so  $L_{MO}/h$  dropped to values less than -1. Temperature decreased, and the diurnal thermocline descended further. Subsequently,  $L_{MO}/h$  increased to values just below 0, indicating cooling with negligible winds. Temperature continued to decrease, with the rate differing between stations. If the diurnal thermocline did not reach the bottom during the windy period, it did during this later period. The tight relation between changes in thermal structure and  $L_{MO}/h$  indicates the strong sensitivity of thermal structure to changes in heating and cooling relative to wind speed. Figure 4.7 show a summary of the conclusions drawn for the ratio  $L_{MO}/h$ .

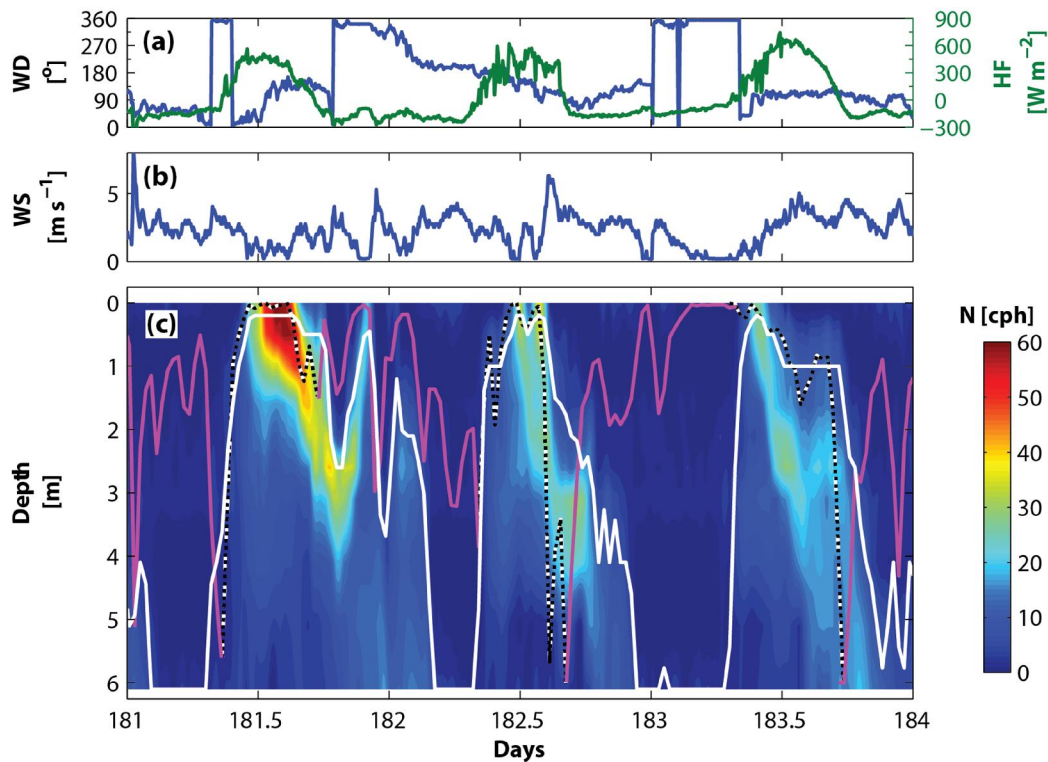
Figure 4.7: Summary of the periods identified by the ratio  $L_{MO}/h$ .



These patterns are further illustrated for the three-day time series from days 181 to 183 (Figure 4.8) during which the change in the midday pattern in  $L_{MO}/h$  occurred. That is, on day 181 it stayed near 0 for several hours, fluctuated between 0 and 1 on day 182, and was persistently above 1 during the period with greatest heating on day 183. Stratification, quantified as the buoyancy frequency ( $N$ ), reached 60 cycles per hour (cph) and remained that high for several hours during midday heating on day 181;  $N$  was slightly less at the surface and briefly depressed in response to a slight increase in winds on day 182. On both these days, the strong near-surface stratification persisted for several hours and the water column was linearly stratified to 2.5 m. In contrast, when  $L_{MO}/h$  was above 1 during morning and afternoon heating on day 183,  $N$  only increased to 25 cph and remained that high for a short period. Subsequently  $N$  dropped to  $\sim 5$  cph and the actively mixing layer deepened. The upper water column was responsive to wind and changes in wind direction despite the stratification. On each of the days, the diurnal thermocline downwelled with increased wind and upwelled on relaxation. For example, on day 181, when winds increased to  $4 \text{ m s}^{-1}$  in late afternoon, the diurnal thermocline deepened to 3 m and rebounded to the surface as the wind ceased. With the near-surface temperatures of  $31^\circ\text{C}$  and temperatures below the diurnal thermocline  $29^\circ\text{C}$ , the diurnal thermocline at 1 m, and letting fetch be 4 km, the Wedderburn number was 0.1 when wind speed increased. This low value implies that wind contributed to mixing by inducing shear across the thermocline as well as near surface currents. The weakened stratification by later afternoon on all days resulted from wind induced mixing and from heat loss as solar

radiation decreased and the effective heat flux shifted to negative values (Figure 4b). Overall stratification was greater in the later period on day 183 when more heat had been mixed downwards with the persistent afternoon winds. The combined forcing which moderates the intensity of stratification is quantified by use of  $L_{MO}/h$ .

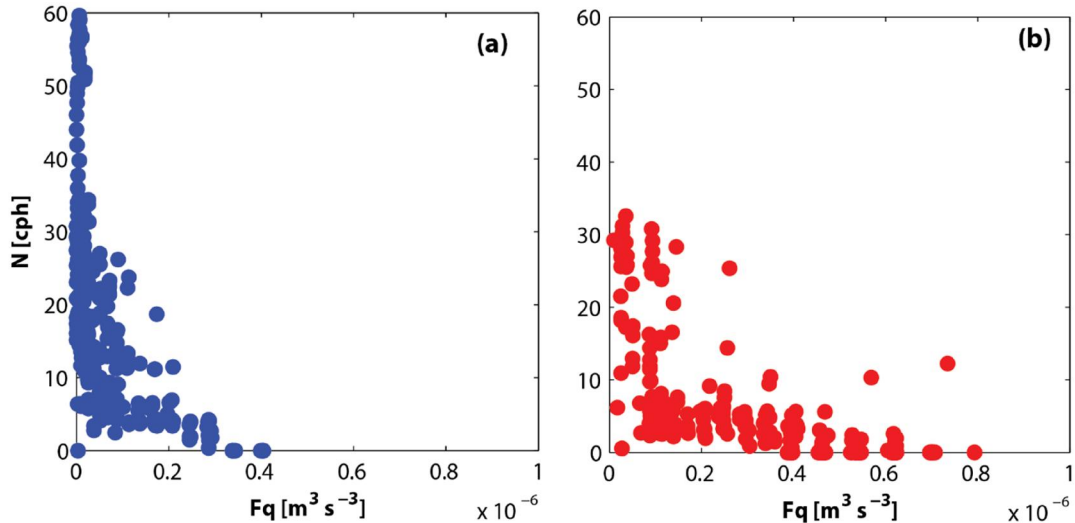
Figure 4.8: Five-minute time series of (a) wind direction (WD, blue, left axis) and effective heat flux into the actively mixing layer (HF, green, right axis); (b) wind speed (WS); and (c) time-depth diagram of buoyancy frequency ( $N$ ) in cycles per hour (cph) for days 181 to 184 at station 2. The white line marks the depth of the actively mixing layer, the magenta and dashed black-white lines show  $L_{MO}$  under cooling and heating, respectively.



Temperature in the day and their depth distribution were dependent on the magnitude of  $F_q$  and solar radiation. When  $F_q$  was low and solar radiation high, which also means  $L_{MO}/h$  was positive and approached zero, and the

Wedderburn number exceeded 100 for a wind speed of  $0.2 \text{ m s}^{-1}$ , heat was trapped near the surface. On days when winds were higher in the day and  $F_q$  was  $\sim 10^{-7} \text{ m}^3 \cdot \text{s}^{-3}$ , the Wedderburn number decreased to values below 6, heat mixed more deeply in the water column and the overall temperature was lower. In these cases,  $L_{MO}/h$  was greater than or equal to 1. The dependence of  $N$  on  $F_q$  at Station 2 is illustrated in Figure 4.9. Higher values of  $N$  occurred when  $F_q$  was less than  $10^{-7} \text{ m}^3 \text{ s}^{-3}$ . As can be seen in Figure 4.3, the decreases in  $N$  with higher  $F_q$  resulted from downwelling of the diurnal thermocline and near surface mixing. The patterns which resulted from changes in  $L_{MO}/h$  and  $F_q$  were evident at all stations although there were between station differences in temperature and in  $N$ . For example, when  $F_q$  was low, near surface stratification developed at Station 4, whereas water at that station was nearly isothermal subsequent to day 181 when  $F_q$  was higher due to the consistently elevated winds during both day and night. The influence of solar radiation was magnified on day 178 with its higher cloud cover and rain. Temperature dropped at all stations. The effective heat flux was only above zero for a few hours and was sometimes negative at times when it was positive on other days. Consequently, the water column cooled in the day, and the values of temperature the following morning were the coldest of the study.

Figure 4.9: Relation between the buoyancy frequency ( $N$ , in cph) and  $F_q$  during heating between late morning and mid-afternoon (i.e., 9:30 to 14:30) when the ratio  $L_{MO}/h$  is (a)  $0 < L_{MO}/h < 1$  when light winds yield strong and shallow stratification, and (b)  $L_{MO}/h > 1$  when strong winds caused the weakening of the stratification from downwelling of the diurnal thermocline and near surface mixing.



Differences between site were related to fetch and proximity to the river. Station 1 was located in Lake Poção Grande with the largest fetch and deepest water column. The depth of mixing was greater there and near surface water temperatures were cooler. During the second period, stations 3 and 5 had notably warmer waters than the other two stations in Lake Paranaptinga despite having lower  $K_d$ . Water at these two stations was less turbid as these regions of the lake received overbank flow through a wide belt of flooded vegetation (ARNESEN et al., 2013; RUDORFF et al., 2014, 2018) which trapped suspended sediments and alters  $K_d$  spectrally. The lower temperatures at the two mid-channel sites, stations 2 and 4, likely resulted from their greater exposure to wind or riverine inflows. The deeper diurnal thermoclines at station 2 supports the inference of greater exposure to wind. Station 4 was the station most directly influenced by overbank flow from levee breaches. In comparing

the 3 shallowest stations, the diurnal thermocline was shallower at station 4 in period 1 and temperatures were cooler and thermal stratification least at station 4 during period 2. The rate of cooling varied between stations in the late afternoon and night. For example, temperature decreased more rapidly in the afternoon at stations 2, 4 and 5, and warm water was retained longer and stayed warmer at night at Station 3 located in a shallow embayment. Exposure to wind also moderated upwelling of colder water. Upwelling in early morning was prevalent at stations 1 and 2 in all periods.

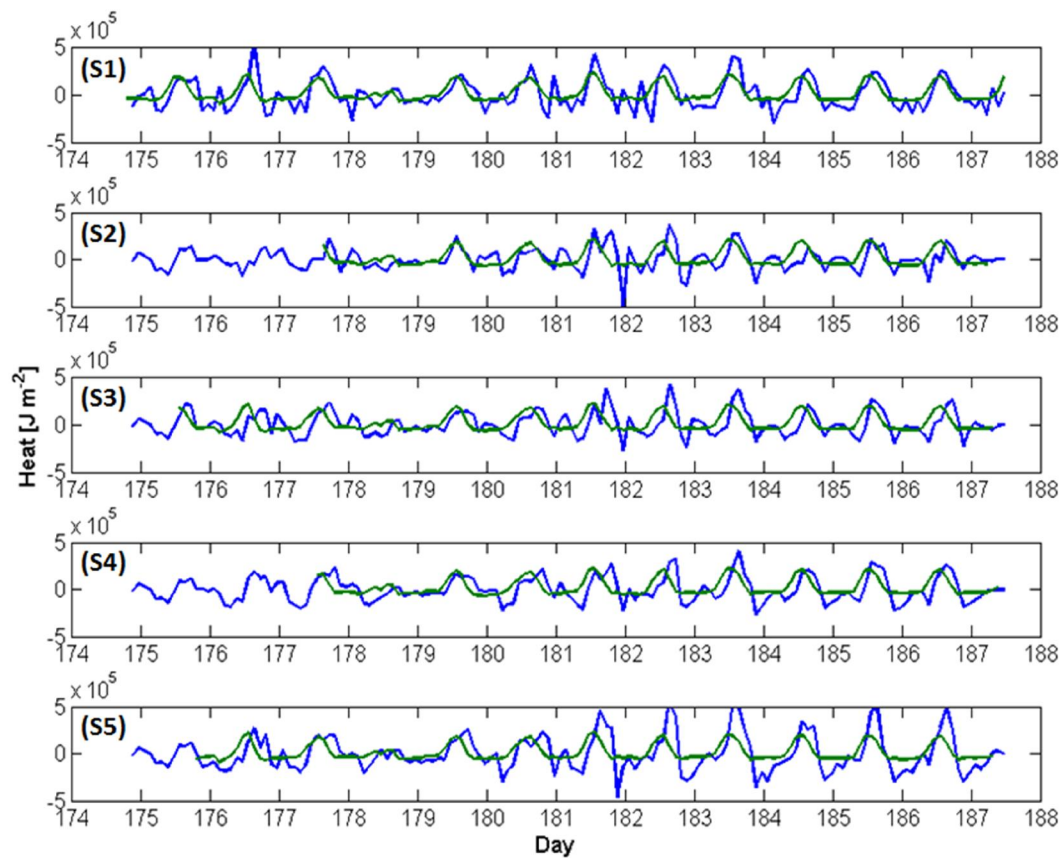
Differences from east to west were also evident in L. Paranaoptinga. With the onset of easterly winds, upwelling occurred at Station 3 to the east. The diurnal thermocline was shallower to the east at station 3 than to the west at stations 2, 4 and 5. This pattern implies a flow of water from the east to the west causing downwelling to the west. While the diurnal thermocline was indeed deeper at station 5 than at station 3, it is not clear that a full basin downwelling occurred as the diurnal thermocline at station 5 was not always deeper than at station 2.

#### **4.2.5 Local changes in heat content versus changes from advection**

To assess whether advection was occurring and moderating the extent of heating and the thermal structure, we contrasted the time series of heat fluxes computed from the surface energy budget with that computed from temperature within the water column,  $Q_M$  and  $Q_T$  respectively (Figure 4.10). Quantitative differences among the heat calculated with those two sources indicates advection, i.e., if  $Q_M$  is larger than  $Q_T$ , colder water is being advected into the

measurement area. The opposite indicates that warmer water is being advected into the measuring area. If the estimated heat from both sources agree ( $Q_M=Q_T$ ), heat content in the water column can be explained based on local forcing.

Figure 4.10:  $Q_M$  (green line) and  $Q_T$  (blue line) for stations (S) 1 to 5. Data are filtered over 2 hours.



For all stations, both  $Q_M$  and  $Q_T$  were relatively similar through day 180. Afterwards, they began to diverge with nighttime  $Q_T$  lower than  $Q_M$  somewhat before midnight and again in the morning. There is a pattern of underestimation  $Q_M$  during periods of high solar radiation, which would indicate that advection is responsible for warmer water input during daylight. In contrast, at the end of

daylight there is a more pronounced decrease in  $Q_T$ , followed by later increase, making it larger than  $Q_M$ , which would mean that colder water is being advected into the sites of measurement.

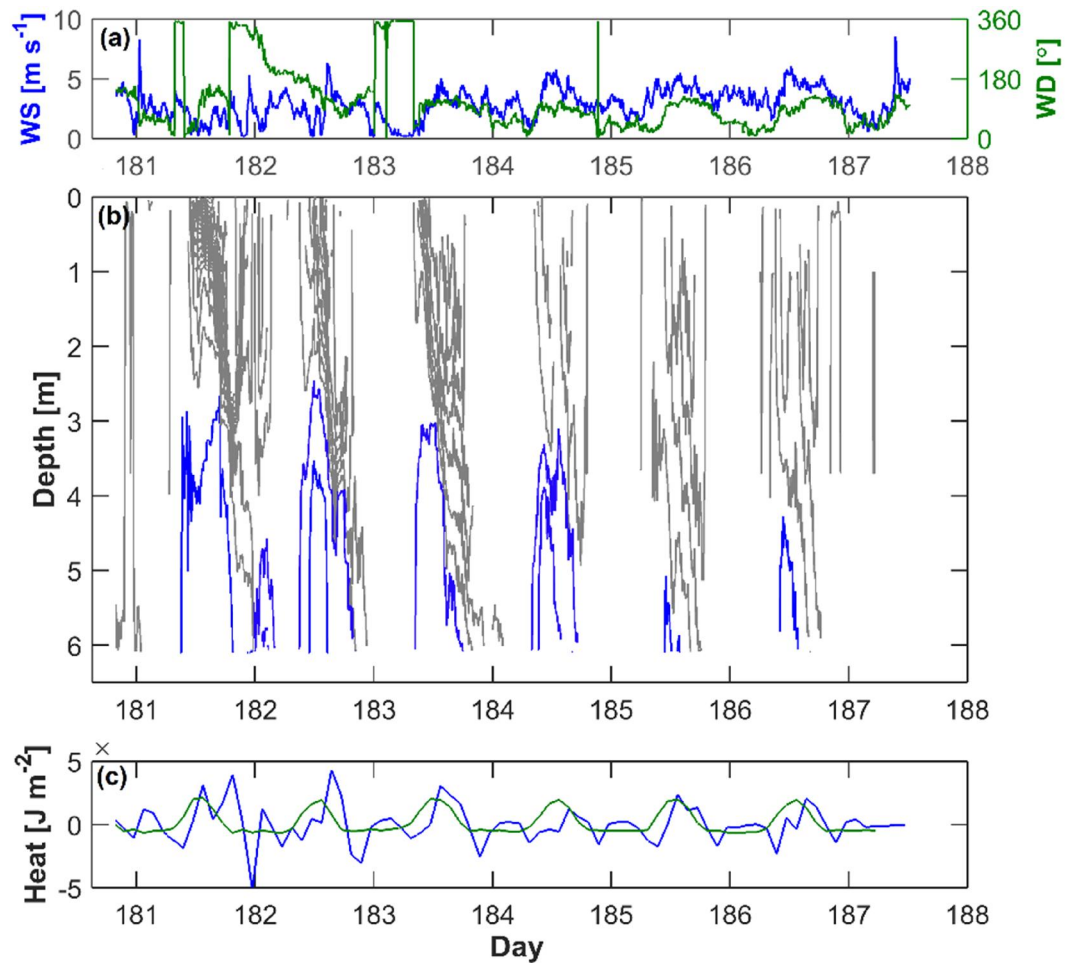
For example, changes in heat content in the water column at station 3 agreed with those computed from the surface energy budget with the exception of oscillations in  $Q_T$  which occurred in response to wind induced up and downwelling of the diurnal thermocline. Values of  $Q_T$  in the afternoon exceeded  $Q_M$  generally with a lag of ~3 hours relative to the peak in  $Q_M$ . This pattern was more pronounced for days 181-183 at all stations and for all the second period at stations 4 and 5.

Despite their differences,  $Q_M$  and the  $Q_T$  were not statistically different for all stations but station 4 (t-test with 1% significance). This means that the only station in which horizontal transport plays a significant role to the heat budget is station 4, which is plausible since this station is the closest to the Amazon River and aligned to a more channelized flow. This explains why station 4 is the only one that can't sustain stratification during daylight.

Regarding stations 1, 2, 3 and 5, the shape discrepancies could rely on tilting in the thermocline due to variations in wind speed and/or direction. An increase in wind speed or a change in wind direction can tilt the thermocline and warmer water is pushed downwards. As the wind weakens or its direction changes, the thermocline relaxes, and colder bottom water is brought closer to the surface, i. e. upwelling. This process is represented in Figure 4.11 for station 2: in days 181 and 183, changes in wind direction are responsible for tilting the

thermocline and causing the upwelling of colder water from the bottom; in days 182 and 184, changes in wind speed are responsible for the same process.

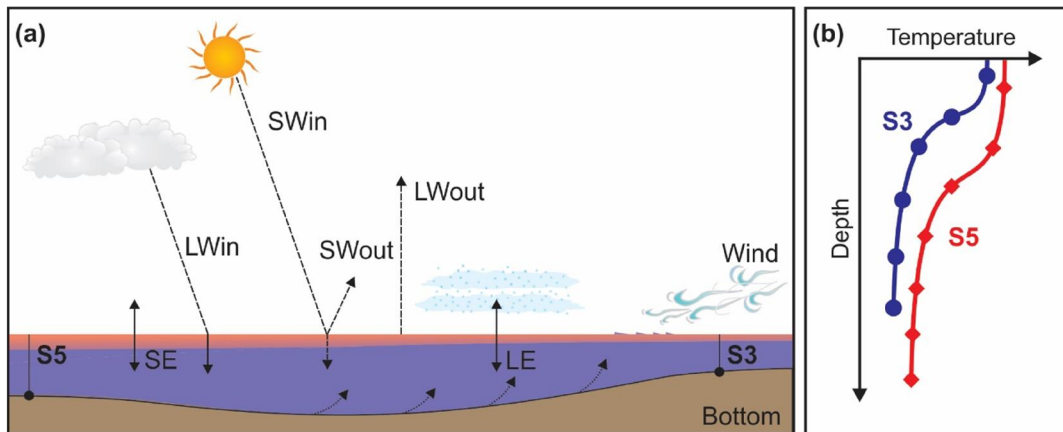
Figure 4.7: Example from station 2: (a) Wind Speed (WS) and Wind Direction (WD); (b) Isotherms where blue lines indicate upwelling; and (c)  $Q_M$  (green line) and  $Q_T$  (blue line).



Upwelling occurs in station 1, 2 and 3. Its major magnitude occurs in station 1 due to its large wind fetch and bottom topography, which creates conditions for the upwelling to reach the surface of Lake Poço Grande. Upwelling is weaker in station 3 due to its lower wind fetch and its location in an embayment. The

only station among the ones not affected by advection in which upwelling does not occur is station 5. Its upwind location does not favor the occurrence of upwelling and wind may displace warmer water towards it. At this station, wind comes from east displacing warmer water of the surface layer from chain 3 towards chain 5. As result of this displacement and bottom topography, upwelling would occur in chains 2 and 3 sites and generate conditions to intrusion of solutes from the hypolimnion and resuspension of sediments (Figure 4.12). Despite that, its lower  $K_d$  favor a faster loss of water heat content once sunlight ceased.

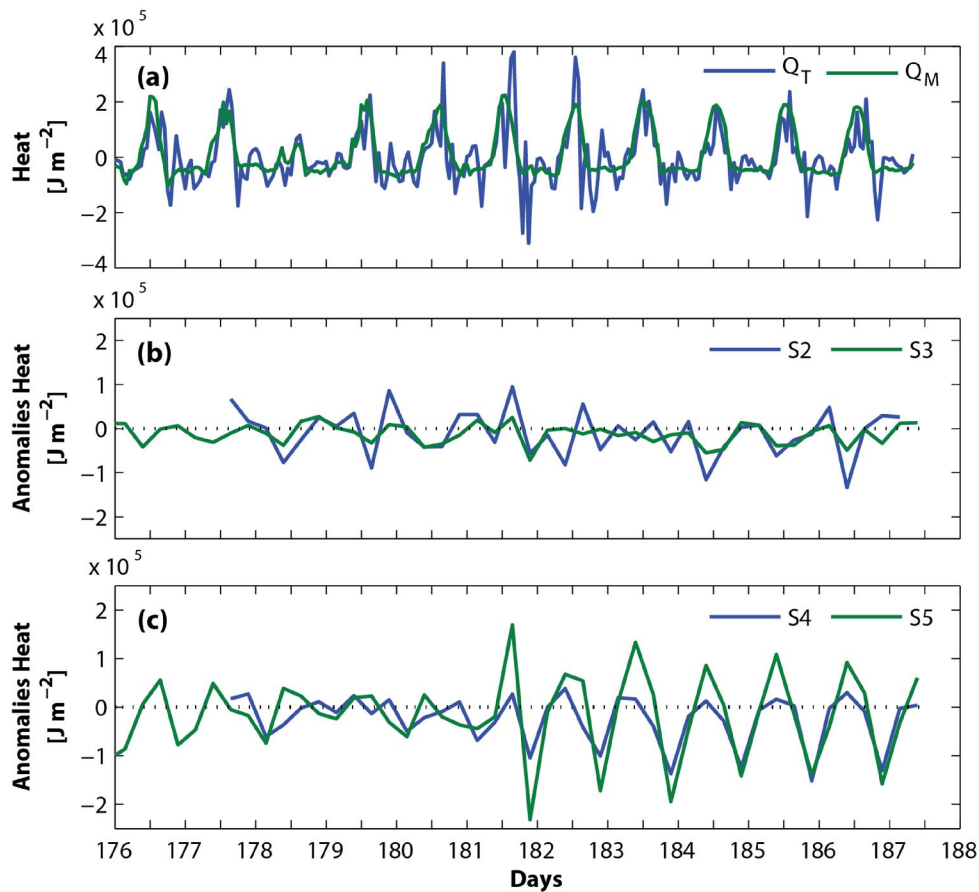
Figure 4.8: (a) Transect in the main wind direction from station 3 (S3) to station 5 (S5) showing the main components of the heat budget. Arrows coming from the bottom towards the surface layer represent the upwelling of cold water from the hypolimnion as the wind is tilting the thermocline in the main wind direction (from East to West); (b) Temperature profiles for Stations 3 and 5 at 13:00 (local time).



To highlight the differences between stations and to remove the influence of short-term wind events, we computed anomalies by subtracting  $Q_M$  from  $Q_T$  and averaging over 6 hours (Figure 4.13).  $Q_T$  at station 2 also tended to be similar to  $Q_M$  with a few divergences. During the first period of the study,  $Q_T$  and  $Q_M$  were

similar at stations 4 and 5. More pronounced differences occurred in the second period of the study with its sustained winds. These included greater heat gain at station 5 in the day, with the concurrent heat losses sometimes occurring at station 2. They also included greater heat loss at night at both stations. Proximity to the Amazon River and differences in wind exposure and basin morphometry are likely to have led to differences between station regarding the magnitude of the anomalies.

Figure 4.9: (a) Hourly heat content per unit area estimated from temperature in the water column,  $Q_T$  (blue line), and computed using meteorological data,  $Q_M$  (green line) at station 3. (b) Anomalies between the observed heat content in the lake and that predicted from meteorological data ( $Q_T - Q_M$ ) at stations 2 and 3 (blue and green, respectively); (c) As in panel b except for stations 4 and 5.



### 4.3 Discussion

The data from the five thermistor and meteorological arrays in Lakes Poço Grande and Paranatinga illustrate the diel cycles of diurnal stratification and nocturnal mixing and the differences between sites moderated by advection, basin morphometry, and wind exposure. The analyses illustrate how daily to weekly changes in meteorological forcing, fetch, and advection moderate the mixing dynamics and induce spatial variability. It was shown that diurnal stratification and near-surface temperature was high in the day when winds and resulting flux of turbulent kinetic energy,  $F_q$ , was low,  $10^{-9} \text{ m}^3 \text{ s}^{-3}$ . In contrast, even for low to moderate winds of  $3 \text{ m s}^{-1}$  to  $5 \text{ m s}^{-1}$ ,  $F_q$  was 2 to 3 orders of magnitude higher and heat was mixed deeper in the water column. Transitions in thermal stratification occurred in response to changes in wind and buoyancy flux parameterized by  $L_{MO}/h$ . Up and downwelling were prevalent features in the day despite vertical mixing's reaching to the bottom at night. Changes in wind direction even when winds were light could induce upwelling. Like other tropical lakes, latent heat fluxes dominated the surface energy budget and the turbulent velocity scale due to convection tended to be larger than that from wind under cooling (MACINTYRE et al., 2002). At night,  $F_q$  reached  $10^{-6} \text{ m}^3 \text{ s}^{-3}$  when winds were moderate under cooling, and only fell by an order of magnitude when winds decreased. Consequently, nocturnal mixing and cooling were sustained by convection.

Vertical mixing tended to reach the bottom in comparison to previous studies in lakes in the central Amazon floodplain that sustained seasonal stratification at high water (LAKE CALADO; LAKE JANAUCÁ – MELACK; FISHER, 1983;

MACINTYRE; MELACK, 1984; LAKE CRISTALINO; LAKE JACARETINGA - TUNDISI et al., 1984). The only Amazon floodplain lake previously reported to fully mix at diel time scales during high-water was Lake Batata (MELO et al., 2004), where the mixing was hypothesized to be a response to advection from riverine overbank flow. However, wind and water speed were not sampled during their study to allow a more conclusive investigation.

Advection was caused by several processes. Wind induced tilting of the diurnal thermocline and resulting up and downwelling was one source of advection. On upwelling, cool water rose towards the surface with the extent of upwelling larger where fetch was greater. Warmer water flowed to our measurement sites on downwelling. That said, spatial variability in temperature indicated that the wind induced downwelling was not necessarily cross-basin as in other lakes but was over smaller spatial scales. Incoming river water was another cause of advection. Velocities as river water flowed over the banks were high. Overbank flow from the river is presumably turbulent near levee breaches and distributary channels. While current speed at measurement sites was smaller than those measured near the river, depth averaged currents ranged from 0.10 to 0.17 m s<sup>-1</sup> (Table 1) which is still appreciable and could contribute to mixing. Additional measurements would be required to quantify spatial and temporal variations in  $F_q$  from bed shear stress on this floodplain.

Overbank flow from the Amazon River moves on the floodplain primarily to the southeast with some local variability presumably due to topographic steering as at station 3 where it flows to the southwest. The floodplain topography is higher in the northwestern region of overbank deposits and lower in the interior of lake

basins. The variation in bathymetry has the potential to induce spatial differences in surface water temperature with warmer water expected to form over the shallow regions and cooler water at night. The process of warm water flowing offshore as a buoyant overflow is known as differential heating and the converse is differential cooling (MONISMITH et al., 1990). Flows from these processes may lag the maximum in heating and cooling by several hours. The notably warmer water at night at station 3 may be a result of the warmer nearshore water flowing offshore where it subsequently cooled. Advection of cool water from inshore to offshore provides an additional mechanism besides the transports from up and downwelling to explain why  $Q_T$  dropped below  $Q_M$  at night at station 5. Both stations 3 and 5 are of order 1 km from shallower, vegetated regions. With average flow speed of  $0.15 \text{ m s}^{-1}$ , the time scale for advection was  $\sim 2$  hours, like the time lag between heating from the surface energy budget and that measured in the lake. This calculation supports the arguments for advection moderating the within lake heat budget. Thus, while our analysis of the heat budgets indicated up and downwelling contributed to advection, between site differences in temperature and rates of heating and cooling indicate the additional influences of basin morphometry and proximity to the Amazon River.

Advection and the extent of vertical mixing also varied with cloud cover and the associated modifications in weather patterns. For example, the cloud cover on day 178 was extensive and easterlies only occurred during the brief heating periods. During a brief period with  $L_{MO}/h$  positive and equal to 0.5 in the early morning, slight warming occurred near the surface. With  $L_{MO}/h$  positive but

greater than 1 for about two hours in mid-afternoon, the incoming heat was rapidly mixed downwards such that near surface stratification was minimal. Late afternoon was characterized by cooling with high winds and then cooling at night. From mid-afternoon onwards, temperature decreased at all stations over this period and were uniform with depth. The coldest temperature of the study was observed by early the next morning. With the continued cloud cover over these two lakes, heat did not accumulate elsewhere and, in contrast to other days, warm water was not advected with changes in wind direction in late afternoon. In fact,  $Q_T$  and  $Q_M$  were similar and low on day 178 except during early morning cooling. The more negative  $Q_T$  at that time implies advection of cooler water, and, as can be seen in Figure 12, upwelling occurred in the lower water column. However, the source of the water is unclear. Based on wind direction, cooler could have come from the south. However, with sustained flow from the north, there might have been intrusions of river water. Regardless, with  $L_{MO}/h < -1$ , the upwelled water would have mixed with ambient. Thus, the colder water temperature, as observed early on day 179, resulted not only from surface cooling but also from mixing of the cool water which had upwelled 24 hours earlier. From this analysis, as well as the earlier discussion of up and downwelling, the water which is mixed vertically at night has generally come from another region within the lake.

The diel mixing dynamics in the two lakes studied are more complex than those in tropical Kranji Reservoir, Singapore (XING et al., 2014). Three physical forcing regimes were identified in the reservoir: a solar radiation-dominated regime, a windy-regime and a cold inflow-regime. Lakes on the Curuai

floodplain are subjected to diffusive overbank inflow from the Amazon River into the floodplain, whereas Kranji Reservoir has channelized inflows from tributaries. In addition, Kranji's area is about 1% of the area of the lakes studied here, and the distance from the river to the closest station in Lake Paranaatinga is larger than the main watercourse of Kranji Reservoir as a whole. Using the ratio  $L_{MO}/h$ , four regimes dominated the lakes studied: (i) solar radiation tended to co-occur in the morning with light winds resulting in shallow stratification,  $0 < L_{MO}/h < 1$ ; (ii) in the afternoon, concomitant heating and higher winds caused the diurnal thermocline to tilt downwards and some heat to mix to deeper layers,  $L_{MO}/h > 1$ ; (iii) by late afternoon,  $B$  became negative and  $L_{MO}/h < -1$  and, as shown by the comparisons of  $u_{*W}$  and  $w_*$ , mixing from wind and cooling co-occurred part of the afternoon and night; and (iv) convection dominated on nights with light winds,  $-1 < L_{MO}/h < 0$ . Differences between the two periods that characterized this experiment were more intense during the afternoon where  $L_{MO}/h > 1$ . During the second period heat could be mixed to deeper layers than during the first period (before day 181). At station 4 conditions were similar to those in Kranji Reservoir where mixing from advection introduced cooler water, which is supported by the statistical analysis of  $Q_M$  compared to  $Q_T$ . For the sites which are closer to the river such that incoming water flowed over shallow, vegetated sections, the diffuse attenuation coefficient was lower than at the more wind exposed sites. Despite the smaller  $K_d$ , temperature in the day were often warmer than at the other sites. Additionally, water was cooler at night and warmer in the day than expected from up and downwelling. We hypothesize that heating and cooling were greater at the shallow regions upstream of these

sites, and the cooler nighttime temperature resulted from the flow of cooler water from shallow regions offshore, and the warmer water in the day similarly resulted from the flow of warmer water from the shallower regions. The presence of vegetation may have contributed to the warming by reducing winds and, consequently, evaporative cooling. Thus, the thermal stratification in tropical lakes Poço Grande and Paranatinga was moderated by more processes than documented in the tropical reservoir.

#### 4.3.1 Nocturnal convection

At night, the turbulent velocity scale for cooling,  $w_*$ , often exceeded that from wind,  $u_{*W}$ . Penetrative convection,  $w_*$ , often reached  $0.01 \text{ m s}^{-1}$  at night and was often twice the value of  $u_{*W}$ . Consequently,  $h/w_*$  was less than  $h/u_{*W}$  indicating that thermals from cooling will more rapidly mix the actively mixing layer than eddies from shear. Thus, in contrast to predictions that mixing will be dominated by shear in larger lakes, convection makes a large contribution to mixing, in part due to warm surface temperature and in part due to the unstable atmosphere above the lake which increases mass transfer coefficients at low winds and thus sensible and latent heat fluxes. A larger  $w_*$  is often interpreted to mean that near surface turbulence would be energized by convection and the gas transfer coefficient, which is determined from rates of dissipation of turbulent kinetic energy  $\epsilon$ , would depend on the rate of cooling,  $B$  (READ et al., 2012). However, care must be taken with this interpretation since near surface dissipation of turbulent kinetic energy follows law of the wall scaling at wind

speed similar to those in this study (TERRAY et al., 1996). Law of the wall scaling implies that  $\epsilon$  depends on  $u_{*W}^3$  divided by the von Karman constant, 0.4, and depth. Thus,  $\epsilon$  is highest near the surface and decreases with depth. The magnitude of  $\epsilon$  also depends on  $B$  (LOMBARDO; GREGG, 1989; TEDFORD et al., 2014). The contribution of  $u_{*W}^3/0.4z$  and  $B$  to dissipation rates are only equal at the depth of  $L_{MO}$ . Thus, the expectation is that if there is even light wind, shear will dominate turbulence production near the surface and  $B$  will dominate turbulence below  $L_{MO}$  (TEDFORD et al., 2014).

However, with their warm surface water temperature,  $B$  under cooling can be more negative in tropical water bodies than temperate and arctic ones for the same wind speed (MACINTYRE; MELACK, 2009). Consequently, the contribution of  $B$  under cooling to dissipation rates could exceed that from the shear production term. To test this hypothesis, we determined if  $B > u_{*W}^3 / 0.4z$ . The coefficients in Tedford et al. (2014), both of which are of order 1, were neglected. For conditions at station 2 under cooling and letting  $z$  be a near-surface value of 0.15 m,  $u_{*W}^3/0.4z$  ranged from  $10^{-9} \text{ m}^2 \text{ s}^{-3}$  to  $10^{-4} \text{ m}^2 \text{ s}^{-3}$ .  $B$  was larger than  $u_{*W}^3/0.4z$  as the latter decreased below  $10^{-7} \text{ m}^2 \text{ s}^{-3}$  when winds were less than  $1.0 \text{ m s}^{-1}$ . At such times, the mass transfer coefficients used to calculate latent and sensible heat fluxes increase up to two and a half times those under the neutral conditions found at higher wind speed. Thus, despite winds decreasing sensible and latent heat fluxes are sustained such that  $B$  may dominate turbulence production at very low winds. These results imply that near surface turbulence will be sustained by cooling and that the calculation of

gas transfer coefficients can be based on  $B$  alone, assuming  $B \approx \epsilon$ , in the surface renewal model (ZAPPA et al., 2007; MACINTYRE et al., 2010). That said, comparative studies with direct measurements of fluxes and of turbulence under cooling are required to determine the depth at which this comparative calculation should be done. Results from a small arctic pond similarly show turbulence sustained by convection, although in that case when winds were negligible and surface currents had ceased (MACINTYRE et al. in press). In floodplain lakes, sustained flows from the river may induce more near-surface turbulence than convection. The advective flows as winds shift direction and from differential heating and cooling may also produce near-surface shear. While one can compute  $u_{*W}$  and  $w^*$  from the surface energy budget, the presence of sustained flows implies the need to quantify the near-surface turbulence from these other processes and include the additional sources of turbulence when computing gas transfer coefficients.

#### **4.3.2 Biological and biogeochemical implications**

Even during high flood stage, the large lakes on the lower Amazon floodplain undergo diel cycles of diurnal stratification and nocturnal mixing. Proximity to the river, changes in bathymetry and vegetation, and wind induced up and downwelling provide additional controls and cause spatial variability in temperature and stratification. The persistent stratification in the day separates the water column into regions with differences in light supply and organic matter. For example, during stratification, near-surface phytoplankton can receive sufficient light to support growth despite high  $K_d$ . The drawdown of

oxygen and accumulation of CO<sub>2</sub> in the lower water column may be appreciable such that nocturnal mixing can reoxygenate the water column and bring water enriched in CO<sub>2</sub> to the air-water interface. Near surface concentrations of dissolved gases will vary in space and time. Additionally, as near surface turbulence is computed based on Monin-Obukhov similarity scaling, the diel variability in near surface  $z/L_{MO}$  implies temporal variability in dissipation rates and gas exchange coefficients. Additional variability is likely induced by other processes causing near surface shear. The combination of temporally varying dissolved gas concentrations and gas exchange coefficients needs to be considered when computing evasion of climate forcing trace gases (RUDORFF et al., 2011).



## **5 ASSESSING REMOTE SENSING APPLICABILITY FOR EXTRACTING DIRECT ESTIMATES OF WST IN FLOODPLAIN LAKES OF THE LOWER AMAZON RIVER AT HIGH DISCHARGE**

In Amazon floodplain lakes, periodic lateral overflow (BONNET et al., 2008) of the Amazon river modifies sediment transport (RUDORFF et al., 2018), carbon and nutrient cycling (ENGLE; MELACK, 2000; RUDORFF et al., 2011; SCOFIELD et al., 2016), and alters optical properties of aquatic systems (SANDER DE CARVALHO et al., 2015) and it is assumed that these have implications on water temperature, and therefore on stratification in lakes (MACINTYRE MELACK, 2009; MACINTYRE et al., 2009, 2014; AUGUSTO-SILVA et al., 2019).

Under similar wind speed, the warmer surface of tropical lakes causes evaporation rates to be higher than those occurring in high latitude lakes. This warmer surface causes deeper mixing of the water column when solar radiation is reduced (MACINTYRE; MELACK, 2009) making cloud cover an important driver of vertical mixing and latent heat fluxes (TALLING; LEMOALLE, 1998; MACINTYRE et al. 2002, 2014). In turn, vertical mixing affects biogeochemical processes (PATTERSON, 1991), gas exchange at the air-water interface (MACINTYRE et al., 1995; 2010), and the development of hypoxia (BOUFFARD et al., 2013) with implications for fish habitat.

One of the many inputs required to study the physical limnology of a lake is water surface temperature (WST). Several limnological studies showed that the WST of inland water bodies is a good indicator of climate change (ADRIAN et al., 2009; LIVINGSTONE, 2003; WEYHENMEYER et al., 2017). Due to water

high heat capacity, small changes in its temperature can cause adverse effects on the duration of stratification, influencing the development of algal blooms and oxygen depleted zones (LIVINGSTONE, 2003; SAHOO; SCHLADOW, 2008; BOUFFARD et al., 2013). As a parameter, WST is also required for calculations of evaporation rates, heat transfer, momentum, and it determines the flux of gases such as carbon dioxide and methane between the water and the atmosphere (EMERY et al., 2001).

Weyhenmeyer et al. (2016) have demonstrated that temperature difference between air and water can be used as a proxy for sensible heat flux ( $Q_H$ ) which, in turn, can be used to evaluate whether the water body will function as a source or a sink of  $CO_2$  and  $CH_4$  to the atmosphere. However, the temperature measurements used to support their study were point based and lacked spatial representativity, which may cause inaccurate estimates of lake properties. Also, *in situ* sampling frequency may not be sufficient to capture significant temporal variability in lake properties. These limitations in spatial and temporal resolution of *in situ* measurements can make it hard to detect changes in variables subjected to wide variation such as WST making the calibration and validation of remotely sensed WST data important. Also, it has been shown that *in situ* measurements of WST can be used to validate temperature fields retrieved from satellite observations (DONLON et al., 2002; THIEMANN; SCHILLER, 2003).

Additionally, an accurate assessment of surface wind speed is required for estimating water temperature based on physical models (EMERY et al., 2001). The state of the art of remote sensing, however, still lacks the required spatial

and temporal resolution for accurate estimates of wind speed over inland waterbodies. Therefore, while this type of model application in studies of inland lakes is not possible, an alternative is the development of empirical models based on the relationship between concurrent measurements of remotely sensed skin temperature and *in situ* bulk surface temperature, complemented with standard meteorological observations.

All targets emit radiation in the infrared and the microwave wavelengths, and the amplitude of these wavelengths vary with the temperature of the target in a way that allows it to be used as a temperature proxy. Li et al. (2013) reviews the status of some remote sensing algorithms for estimating surface temperature from thermal infrared data. They present the theoretical background of the subject along with a survey of the algorithms employed for obtaining surface temperature from space-based measurements acquired by polar-orbiting satellites.

There is a vast literature on the analyses of vertical temperature profiles in the water column of northerly lakes and reservoirs (EUGSTER et al., 2003; EVANS et al., 2008; MACINTYRE et al., 2009; MACINTYRE et al., 2010; READ et al., 2012; TEDFORD et al., 2014; HEISKANEN et al., 2014, PERNICA et al. 2014), and some in tropical lakes and reservoirs (MACINTYRE; MELACK, 1984; MACINTYRE et al., 2002; VALÉRIO et al., 2012; CURTARELLI et al., 2014, 2016; TEDFORD et al. 2014; AUGUSTO-SILVA et al., 2019), but our understanding of WST of inland water bodies is currently limited with regard to Amazon floodplain lakes. Reinart and Reinhold (2008) used MODIS sensor (Moderate Resolution Imaging Spectroradiometers, onboard of NASA's Terra

satellite) to map surface temperature of two large European lakes using Level 2 daytime Sea Surface Temperature products. They had 23 concurrent satellite and in situ measurements (0.5 m depth) and used a linear regression relating the two measurements yielding an empirical model with  $R^2$  equal to 0.9928. Their data set showed a mean absolute difference of 0.41 K between satellite and in situ temperatures. A more recent study from Pareeth et al. (2016) used 62,799 images from 13 polar orbiting satellites with moderate resolution sensors (one of them MODIS) and *in situ* temperature measurements from 0 to 0.5 m depth, along 30 years of observation. They developed a time series of WST for five large lakes in Italy and evaluated this product with *in situ* data using linear models that exhibited high coefficient of determination ( $R^2$ ) for the study lakes (average of 0.97). These two studies reinforce the value of empirical models to relate skin temperature to bulk temperature.

Many sensors can be used to retrieve surface temperature and each one of them has its specific resolutions. Among them, one must recognize the role of MODIS. It provides surface temperature products four times a day (joint capability of Terra and Aqua satellites) with a spatial resolution of 1 km and have been operating since 2000 (Terra satellite), so, it can provide reasonably long temporal series of surface temperature. The remote sensing product used was MOD11A1 from MODIS level 3 V6 onboard of Aqua and Terra satellites (WAN et al., 2015).

Studies focused on hydrology and hydrodynamic modeling may rely on WST from satellite measurements so, the reliability of direct estimates of this parameter without taking into account the parameterization of the scene sensor

coefficients should be studied. Given the extent of the Amazon floodplains (HESS et al., 2015) and ecological significance of the area, this chapter aims to access the remote sensing capability for directly estimating WST inside a floodplain lake during the high water. It has been shown that lakes influence climate at local and regional scales (SAMUELSSON et al., 2010; SUBIN et al. 2012) due to its large thermal inertia, so the hypothesis that guided this chapter was that WST can be estimated based on skin layer temperature measured from space parameterization of the scene coefficients. To test this hypothesis, *in situ* measurements of WST and surface meteorology were acquired and used to calibrate/validate MODIS level 3 surface temperature product. This work has implications to studies of hydrological and hydrodynamical global warming effects which were made based on skin temperature measured from space.

## **5.1 Methods**

### **5.1.1 *In situ* measurements of WST**

Measurements of WST were collected during high water from June 23 to July 6, 2014, designated as day 172 to day 186 using day of the year notation. A thermistor chain was moored at each station (Figure 2.1) and the thermistors (model: U22-001, brand: HOBO, accuracy:  $\pm 0.2^{\circ}\text{C}$ , resolution:  $0.02^{\circ}\text{C}$ ) used in this experiment were deployed at 0.02 m (shaded by a surface float as can be seen in Figure 2) and 0.5 m depth. The thermistors had a response time (90% of a step change in temperature) of five minutes, and the sampling times were synchronized. The thermistors sampled every 30 s. All thermistors were inter-calibrated and compared to high resolution sensors in the laboratory (model:

RBR solo, accuracy:  $\pm 0.002^{\circ}\text{C}$ ). Due to the digitization noise associated with the HOBO thermistors, data were smoothed prior to final inter-calibration.

### **5.1.2 Remote sensing of WST**

The data used was from MODIS sensors. They acquire data in 36 spectral channels from 0.415 to 14.235  $\mu\text{m}$  with a spatial resolution between 250 m and 1 km depending on the product (SAVTCHENKO et al., 2004). Its spectral bands positions, high radiometric sensitivity, and the relatively easy access to acquired data makes it attractive also for limnology applications. It can be used in the study of phytoplankton pigments, suspended particulate matter, dissolved organic matter and water temperature. In this study, the positions of the thermistor chains were crossed with the MODIS images to extract a pixel value of WST and cross it with the median value of WST collected by the thermistor using a 30 minute window (15 minutes before the scene acquisition and 15 minutes after).

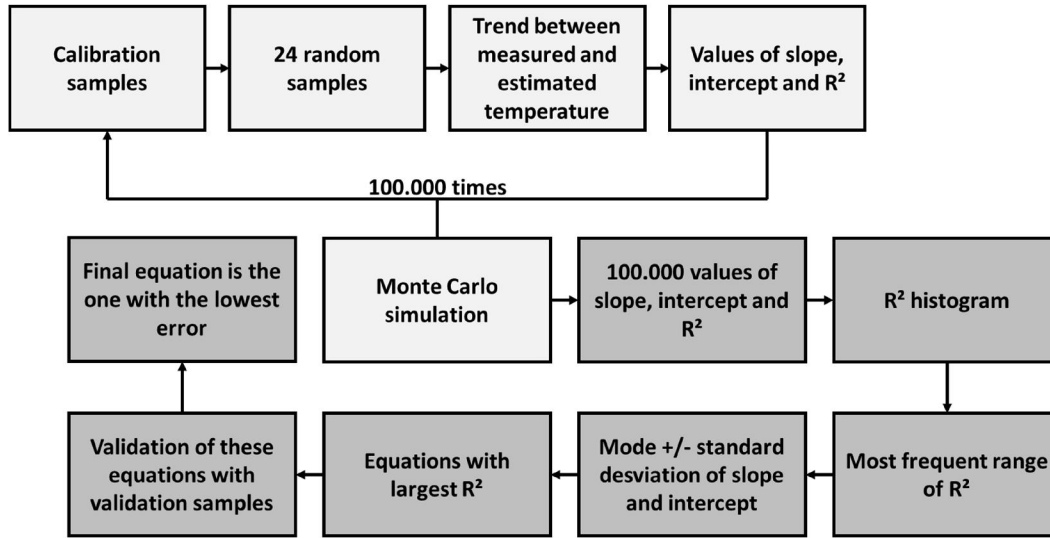
### **5.1.3 Calibration/Validation of the empirical model**

*In situ* temperature measurements from 0.02 m were statistically compared to *in situ* temperature measurements from 0.5 m using a t test for the averages. Following, another t test was applied to verify statistical differences between *in situ* and satellite measurements of WST. Both tests assumed a normal distribution given the number of samples available (n=88). Following, *in situ* measurements from 0.02 m or 0.5 m (hereinafter referred as  $WST_i$  or bulk temperature) were used to adjust WST measurements collected by MODIS

(hereinafter referred as  $WST_M$  or skin layer temperature). All field data were split into quartiles, being used six samples of each quartile for validation. As a result, there were 64 samples for calibration and 24 samples for validation (approximately 30% of the samples available).

A Monte Carlo simulation was performed in the calibration process (Figure 5.1): 24 samples of  $WST_i$  were randomly selected and used to estimate  $WST_M$  using a linear trend. This process was repeated 100 000 times. The resulting values of slope, intercept and determination coefficient ( $R^2$ ) were recorded for each iteration. The  $R^2$  histogram was a decision tool to find the equations which had this parameter in its most frequent range. Within this range of  $R^2$ , we plotted the corresponding slope versus intercept of the equations and determined their mode and standard deviations. Only the equations that had both slope and intercept in a range based on their mode (mode  $\pm$  standard deviation) were selected. From this group, the equations that had the largest  $R^2$  were selected and validated using the validation samples. The equation with the lower error estimator was chosen as the best.

Figure 5.1: Flowchart of the calibration/validation of the WST model using a Monte Carlo simulation.



The error estimators used in this study were: Root Mean Square Error (RMSE); and Normalized Root Mean Square Error in percentage (NRMSE%). They were calculated according to Table 3 and the error estimator used to choose the best equation was NRMSE%, because it represents the impact of the error within the range of the WST measurements.

Table 5.1: Summary of the error estimators used. Where:  $y_i$  and  $x_i$  are  $WST_M$  and  $WST_i$  respectively in each  $i$  sample.

---


$$MSE = \frac{1}{n} \sum_{i=1}^n (y_i - x_i)^2 \qquad RMSE = \sqrt{MSE}$$


---


$$NRMSE\% = \frac{RMSE}{\Delta T} \cdot 100$$


---

## 5.2 Results

### 5.2.1 Meteorology

As shown in chapter 4 of this document, the period of *in situ* data acquisition can be divided into two weather patterns. The first weather pattern, prior to day 181, is characterized by cooler nights and greater cloud cover during the day compared to the second period. In the first period, the air temperature was 3°C cooler than surface waters and in the second, 2°C colder. Relative humidity at night was lower in the second period with its reduced cloud cover, and the pattern of low winds at night from the north and elevated winds in the afternoon from the east was more consistent. Peak wind speeds were  $\sim 5 \text{ m s}^{-1}$  for both periods. Winds more frequently dropped to the instrument threshold at night during the first period. Day 178 differed from the others in that it was overcast with high relative humidity, low shortwave radiation, and showers occurrence with 12.4 mm of rainfall in the morning and 2.2 mm in the afternoon (data not shown). Winds reached  $10 \text{ m s}^{-1}$  during rain storms.

Air temperature ranged from 23.9°C around midnight to 31.1°C around 13:00 (local time) and had an overall mean of 27.9°C (Figure 4.1a). Surface water temperatures tended to be warmer than air temperatures except for a few hours in the afternoon for about half the days (Figure 4.1a). Shortwave radiation reached  $1000 \text{ W m}^{-2}$  at noon under clear sky conditions and varied rapidly in response to changes in cloud cover (Figure 4.1b). Relative humidity was lowest at midday (minimum of 69%) and peaked around midnight (maximum of 95%) with a mean of 82% (Figure 4.1e).

## 5.2.2 Water surface temperature patterns

The analysis of *in situ* measurements of WST among the stations corroborates with the division of the sampling period into two weather patterns: prior to day 181 there is no evident pattern of  $WST_i$  (Figure 5.2), but it is clear that less heat reach water surface on day 178, which, according to meteorology records, was an overcast day with rain; from day 181 on, maximum temperature values decrease until the end of the experiment (Figure 5.3). Also, stations 3 and 5 become warmer than stations 1, 2 and 4 for the second period of the experiment and, from day 182 on, station 4 becomes the coldest with a very cohesive behavior.

Figure 5.2: WST from all sampling stations from day 175 to the end of day 180.

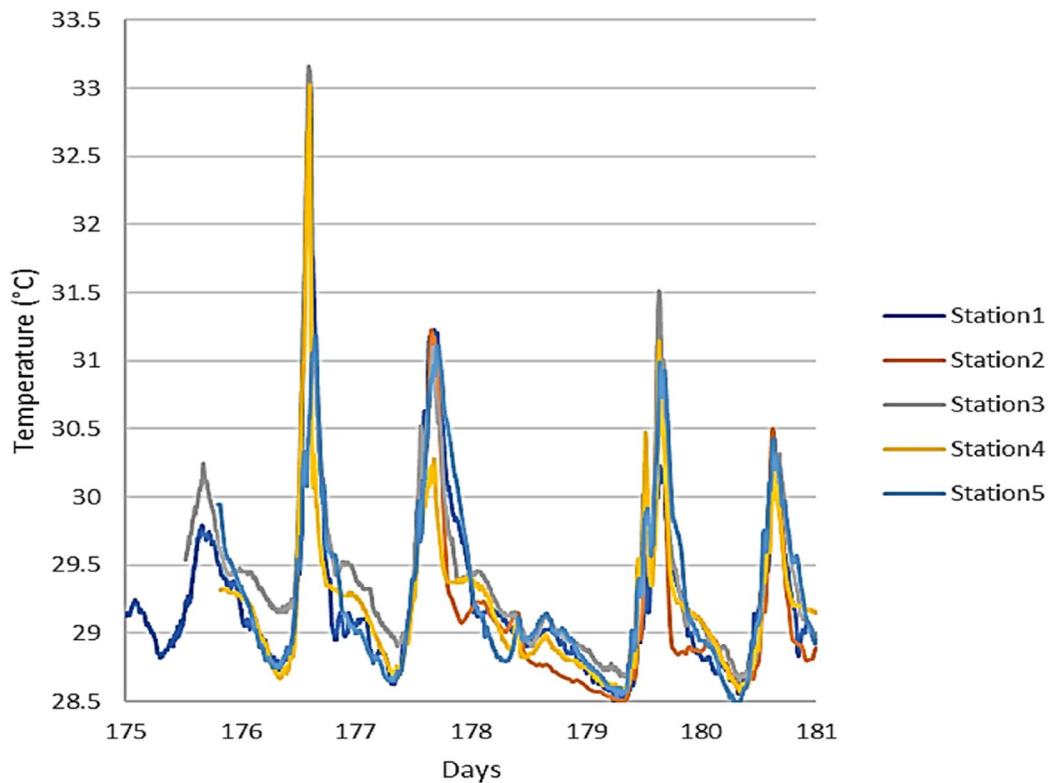
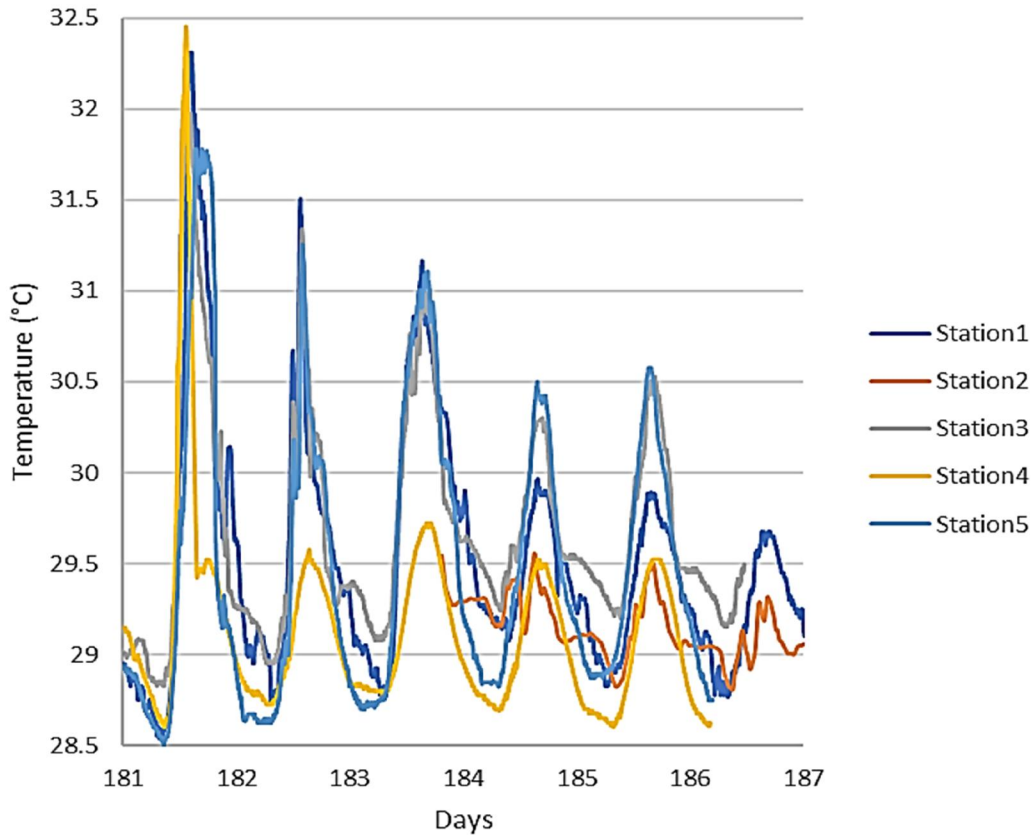


Figure 5.3: WST from all sampling stations from day 181 to the end of day 186.

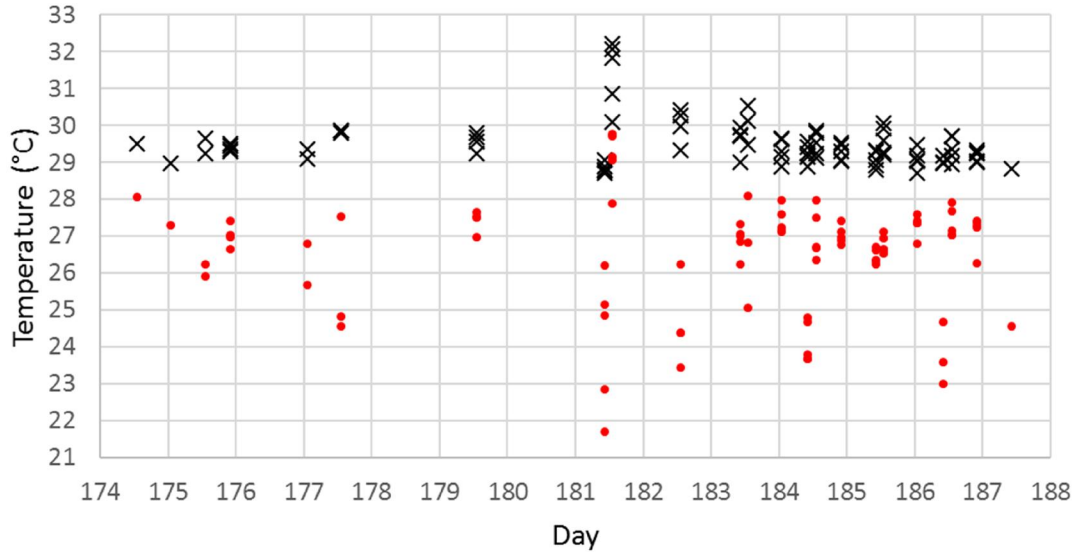


A t test was applied to test the equality of WST measured *in situ* from 0.02 m and 0.5 m depth. It was proven that these measurements are statistically equal for their averages ( $\alpha$  equals to 1% significance). Given this result, *in situ* temperature measurements from 0.02 m depth were used as bulk temperature (or  $WST_i$ ).

Since the first period had greater cloud cover, only three days had concomitant  $WST_i$  and  $WST_M$ , which was not enough for analyzing temperature patterns according to the two weather patterns. During all the sampling period, MODIS temperature data always underestimate WST by at least 0.96°C at 13:00 (local

time, measured by MODIS onboard of Aqua satellite) on day 181, reaching 7.6°C at 10:00 (local time, measured by MODIS onboard of Terra satellite) on day 181 (Figure 5.4).

Figure 5.4: WST measured in situ ( $WST_i$ , black marks) and measured by MODIS ( $WST_M$ , red dots-no model applied) from all sampling stations from day 174 until day 188.



Morning measurements from MODIS onboard of Terra satellite managed to capture 30 cloudless samples, while the night sampling of this same sensor was able to capture only 15 samples. For MODIS onboard of Aqua satellite, in the afternoon, it was able to capture 45 cloudless samples, while the respective night measurement captured only 17 samples from day 174 to day 187. This shows that the best time for data collection in the region under high water should be around 13:00 h (local time). In the end, MODIS onboard of Aqua satellite was able to collect 50 cloudless samples with concomitant  $WST_i$  measurements and while MODIS onboard of Terra satellite was able to collect 38 samples.

The average difference between  $WST_i$  and  $WST_M$  including all data samples was  $2.99^\circ\text{C}$ , always with  $WST_M$  below  $WST_i$ . Separating and analyzing samples from MODIS onboard of Aqua satellite, the average difference between  $WST_i$  and  $WST_M$  drops to  $2.71^\circ\text{C}$  in contrast to the average samples from MODIS onboard of Terra satellite which had averages equals to  $3.30^\circ\text{C}$ . Samples collected by Aqua satellite had a variance of  $1.62^\circ\text{C}$  while samples collected by Terra satellite had the same statistical parameter equal to  $2.37^\circ\text{C}$ , which would indicate better quality of Aqua sensor. In order to test if MODIS-Aqua samples were actually better than MODIS-Terra, a t test for the difference between skin and bulk temperature ( $WST_i - WST_M$ ) was applied. This test showed that these two datasets (MODIS-Aqua and MODIS-Terra) are statistically equal for their averages ( $\alpha$  equals to 1% significance), therefore for the calibration/validation process, both satellites data were used.

### **5.2.3 Calibration/Validation of remote sensing data**

A t test was used to evaluate if  $WST_i$  and  $WST_M$  were statistically the same and it was proved that there is a statistical difference between bulk temperature and skin layer temperature with  $\alpha$  equals to 1% significance. Given this result, the samples were divided between calibration and validation: 64 samples for calibration and 24 for validation. Following, a Monte Carlo analysis was conducted 100.000 times using a linear trend for  $WST_i$  and  $WST_M$ . The most frequent range of values of  $R^2$  were from 0.1 to 0.2, so all equations within this range were selected. Mode +/- standard deviation of the Slope and Intercept

helped to restrict the number of equations that were then validated. Table 4 shows the results from this calibration/validation scheme. The best result had a Normalized Root Mean Square Error in percentage (NRMSE%) of 18.32% of the range of variation of WST data.

Table 5.2: Coefficients derived from the calibration/validation scheme.

<b>Slope</b>	<b>Intercept</b>	<b>R<sup>2</sup></b>	<b>RMSE (°C)</b>	<b>NRMSE (%)</b>
0.1294	26.0462	0.2	0.61	18.32

#### 5.2.4 Bulk temperature estimated by MODIS

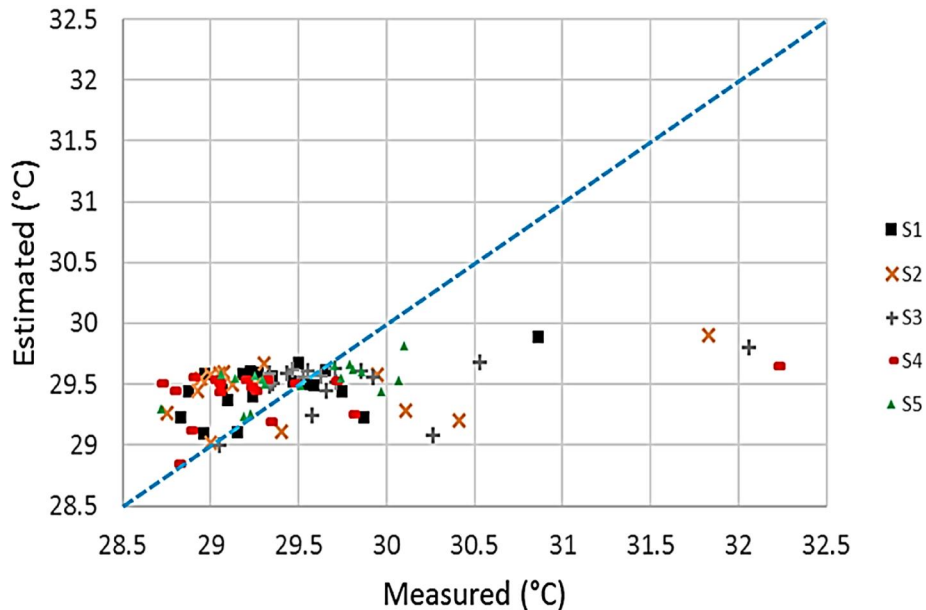
Applying the results from the previous section to MODIS data, it was possible to estimate bulk temperature based on the values collected by MODIS data ( $WST_{Est}$ ). The differences from measured and estimated bulk temperature were analyzed ( $WST_i - WST_{Est}$ ). Major differences were found for day 181 for MODIS-Aqua afternoon measurement: Station 1 had  $-0.97^{\circ}C$ , Station 2 had  $-1.98^{\circ}C$ , Station 3 had  $-2.25^{\circ}C$ , Station 4 had  $-2.56^{\circ}C$  and Station 5 had  $-0.28^{\circ}C$ . The negative sign means that the values estimated based on MODIS measurements ( $WST_{Est}$ ) were higher than those measured *in situ* ( $WST_i$ ). Analyzing synoptically, the mean difference from each station can be found in Table 5. Station 5 has the lower mean difference and station 3 has the higher. Besides that, the mean difference among all stations is low, reaching a maximum of  $-0.27^{\circ}C$ .

Table 5.3: Mean  $WST_i - WST_{Est}$  for each Station.

<b>Station 1</b>	<b>Station 2</b>	<b>Station 3</b>	<b>Station 4</b>	<b>Station 5</b>
$0.10^{\circ}C$	$-0.03^{\circ}C$	$-0.27^{\circ}C$	$0.09^{\circ}C$	$0.01^{\circ}C$

Figure 5.5 was made to help elucidate among station differences. It represents measured temperature and its respective estimated temperature. Line 1:1 in the figure helps to visualize which data is closer or more distant. From this figure, no among station differences were found and the almost horizontal relation between measured and estimated temperature, demonstrates the low capability of MODIS to capture small variations in water temperature. This was expected since  $R^2$  was equal to 0.2, which means that skin temperature only explains 20% of bulk temperature for these study sites.

Figure 5.5:  $WST_i$  and  $WST_{Est}$  separated by sampling Stations (S#, represent the station and its number). Blue dashed line represents 1:1 between measured and estimated temperatures.



### 5.3 Discussion

Differences between skin temperature and bulk temperature were expected since  $WST_i$  was collected 2.5 cm below the water surface and MODIS can

measure only a skin layer of the water surface ( $\sim 10 \mu\text{m}$ , according to NEHORAI et al, 2013), which is the molecular boundary between a water body and the atmosphere. Besides that, *in situ* measurements are point based, while orbital remote sensing data integrates synoptically the information of a pixel, which, in the case of MODIS temperature measurements, have  $1 \text{ km}^2$  of area. Therefore, it is assumed that  $WST_i$  would be statistically different from  $WST_M$ , but it is expected that one can be obtained from the other, i.e, skin temperature should capture variations on bulk temperature and vice versa.

Analyzing  $R^2$  histogram, the most frequent range of  $R^2$  were 0.1 to 0.2, which are low values. This means that bulk temperature explains only 20% of the variability of the skin temperature estimated by MODIS with no parameterization of sensor scene coefficients. Focusing on Slope results, values close to zero indicate that MODIS temperature product is not capable of capturing bulk temperature daily variations for this study area or that the daily variations are not significant to be captured by the sensor. Analyzing the intercept, a positive value of it represents a case where, given a  $0^\circ\text{C}$  of bulk temperature, skin temperature would be positive. The opposite, i.e. a negative value of intercept represents a case where, given a  $0^\circ\text{C}$  of bulk temperature, skin temperature would be negative. Either case, it is not the expected response.

Emery et al. (2001) states that the physical processes that govern the magnitude of  $\Delta T$  (bulk-skin temperatures) can vary with environmental conditions among three regimes: (i) free convection; (ii) forced convection driven by wind stress; and (iii) forced convection driven by wave breaking. They explain that free convection regime dominates at very low wind speeds and the

magnitude of  $\Delta T$  is controlled primarily by the net heat flux. The skin layer continues to cool as a result of the heat flux until it becomes unstable, sinks, and is replaced by warmer water from below. In the second regime,  $\Delta T$  is regulated both by the net heat flux and the wind stress on the surface. The action of the wind on the surface contributes to the renewal of the skin layer and, below it, turbulence acts to create a near-isothermal temperature profile and the magnitude of the turbulence diminishes as it deepens. In the third regime, the surface renewal is dominated by wave breaking and it can be microscale breaking of capillary waves or larger scale wave breaking with air entrainment. During microscale breaking, the skin layer is disrupted for a brief interval and the frequency of the renewal may be largely independent of the wind stress and heat flux. Larger scale wave breaking with air entrainment can mix the skin layer for longer periods of time.

These regimes are not mutually exclusive, they can cooccur and/or happen several times during the same day. Crossing the knowledge of these regimes stated by Emery et al. (2001) with  $L_{MO}/h$  regimes defined in chapter 4 of this thesis, for MODIS sampling period,  $L_{MO}/h > 1$  for MODIS day scenes and  $-1 < L_{MO}/h < 0$  for MODIS night scenes.  $L_{MO}/h > 1$  indicates a heating regime where wind dominates the production of TKE in the actively mixing layer. Since there is heating, skin temperature is supposed to be warmer than bulk temperature, this indicates that the regime that prevails should be forced convection driven by wave breaking. At night, with  $-1 < L_{MO}/h < 0$  convection dominates the production of TKE in the water column, so the regime that prevails should be free convection.



## 6 CONCLUSIONS

Chapter 4 of this thesis was dedicated to investigating how the thermal structure and extent of vertical mixing vary within the lakes studied and what are the physical processes that control it. The ratio  $L_{MO}/h$  was applied to evaluate wind and buoyancy domains in the water column at diel time scales. It was shown that: in the early morning the ratio values were between 0 and 1, which is caused by a combination of both high solar radiation and light winds; by early afternoon the ratio values are more than 1, so there is still persistent solar radiation, which heats the surface layer and wind increases, causing thermocline to tilt, enabling heat to deepen in the water column; by late afternoon, the ratio values were less than -1, which indicates cooling due to both buoyancy and wind; at night, the ratio values stay between -1 and 0 and convection dominates the production of TKE in the water column.

Still in this chapter, the sampling period was divided into two periods regarding weather conditions: first period from day 174 to day 180 had cloudier days and occasional rain; and second period, from day 181 to the end of the experiment on day 187, had clear skies which had higher winds. The main difference between these two periods is SW radiation availability, and the influence of it in the water column was addressed and demonstrates the importance of cloud cover to physical limnology of tropical lakes.

Advection was caused by several processes. Wind induced tilting of the diurnal thermocline and resulting up and downwelling was one source of advection and statistical difference between  $Q_M$  and  $Q_T$  on station 4 (t-test with 1% significance) were the main findings regarding this subject.

From this chapter, it was clear that the main processes that could be systematically monitored through remote sensing would be wind and water temperature, assuming that water temperature is an indicator of heat absorbed by the water. Wind is a source of turbulent kinetic energy in the water column and it can be responsible for erosion of vertical temperature gradients, but, since wind is not a feasible parameter to be evaluated from remote sensing technics, water surface temperature (WST) was the core of chapter 5, which was dedicated evaluate if bulk temperature can be estimated based on skin layer temperature measured from space with no parameterization of sensor scene coefficients. A Monte Carlo simulation was performed, and it was found that, despite having a low normalized error (18.32%), direct estimates of bulk temperature from skin layer temperature cannot be used for hydrological and hydrodynamical studies because, without sensor scene parameterization, MODIS can't capture the whole variation observed *in situ*.

Despite this, it was possible to cross the results from the ratio  $L_{MO}/h$  with regimes that control the difference from skin layer temperature and bulk temperature based on work from Emery et al. (2001) for MODIS sampling period. It was found that  $L_{MO}/h > 1$  for MODIS day scenes, which indicates a heating regime where wind dominates the production of TKE in the actively mixing layer. Since there is heating, skin layer temperature is expected to be warmer than bulk temperature, and the regime that prevails is forced convection driven by wave breaking. For MODIS night scenes,  $-1 < L_{MO}/h < 0$ , convection dominates the production of TKE in the water column, and regime that prevails is expected to be free convection.

Weyhenmeyer et al. (2017) demonstrated that the difference between water and air temperature is a good proxy to sensible heat flux ( $Q_H$ ) and can be used to determine whether a waterbody will act as a source or a sink of  $CO_2$  and  $CH_4$  into the atmosphere. In their work, bulk temperature collected directly in field was used and not skin layer temperature, which would be a remote sensing product. The results shown in chapter 5 of this thesis regarding skin temperature representability of bulk temperature demonstrated the need of sensor scene specific parameterization for the floodplain under study. The obtained model, which was based on direct estimates, presented low  $R^2$  values, indicating that further research is needed on longer time series of the MOD11A1 product collected by MODIS sensor (onboard Aqua and Terra satellites) to allow it to be used for any study.



## REFERENCES

- ABRIL, G.; MARTINEZ, J.-M.; ARTIGAS, L. F.; MOREIRA-TURCQ, P.; BENEDETTI, M. F.; VIDAL, L.; ROLAND, F. Amazon River carbon dioxide outgassing fuelled by wetlands. **Nature**, v.505, n.7483, p. 395–398, 2014.
- ADRIAN, R. Lakes as sentinels of climate change. **Limnology and Oceanography**, v.54, p.2283, 2009.
- AFFONSO, A. G.; BARBOSA, C. C. F.; NOVO, E. M. L. M. Water quality changes in floodplain lakes due to the Amazon River flood pulse: Lago Grande de Curuaí (Pará). **Brazilian Journal of Biology**, v.71, n.3, p.601–610, 2011.
- AMOROCHO, J.; DEVRIES, J. J. A new evaluation of the wind stress coefficient over water surfaces. **Journal of Geophysical Research**, v.85, n.C1, p.433–442, 1980. DOI:10.1029/JC085iC01p00433.
- ANDERSON, E. R. Energy budget studies, water loss investigations - Lake Hefner studies. **U. S. Geological Survey**, v.269, p.71, 1954.
- ARNESEN, A. S.; SILVA, T. S. F.; HESS, L. L.; NOVO, E. M. L. M.; RUDORFF, C. M.; CHAPMAN, B. D.; MCDONALD, K. C. Monitoring flood extent in the lower Amazon River floodplain using ALOS/PALSAR ScanSAR images. **Remote Sensing Environment**, v.130, p.51–61, 2013.
- AUGUSTO-SILVA, P. B.; MACINTYRE, S.; RUDORFF, C., CORTÉS, A., MELACK, J. M. Stratification and mixing in large floodplain lakes along the lower Amazon River. **Journal of Great Lakes Research**, v.45, n.1, p.61–72, 2019. Available from: <http://doi.org/10.1016/J.JGLR.2018.11.001>.
- BOUFFARD, D.; ACKERMAN, J. D.; BOEGMAN, L. Factors affecting the development and dynamics of hypoxia in a large shallow stratified lake: hourly to seasonal patterns. **Water Resources Research**, v.49,n.5, p.2380–2394, 2013. Available from: <http://doi.org/10.1002/wrcr.20241>.

BONNET, M. P.; BARROUX, G.; MARTINEZ, J. M.; SEYLER, F.; MOREIRA-TURCQ, P.; COCHONNEAU, G.; SEYLER, P. Floodplain hydrology in an Amazon floodplain lake (Lago Grande de Curuaí). **Journal of Hydrology**, v.349, n.1/2, p.18–30, 2008. Available from: <http://doi.org/10.1016/j.jhydrol.2007.10.055>.

CARABALLO, P.; FORSBERG, B. R.; DE ALMEIDA, F. F.; LEITE, R. G. Diel patterns of temperature, conductivity and dissolved oxygen in an Amazon floodplain lake: description of a fríagem phenomenon. **Acta Limnologica Brasiliensia**, v.26, p.318–331, 2014.

CURTARELLI, M. P.; OGASHAWARA, I.; ALCÂNTARA, E. H.; STECH, J. L. Coupling remote sensing bio-optical and three-dimensional hydrodynamic modeling to study the phytoplankton dynamics in a tropical hydroelectric reservoir. **Remote Sensing of Environment**, 2014. Available from: <http://doi.org/10.1016/j.rse.2014.06.013>.

CURTARELLI, M. P.; OGASHAWARA, I.; DE ARAÚJO, C. A. S.; LORENZZETTI, J. A.; LEÃO, J. A. D.; ALCÂNTARA, E.; STECH, J. L. Carbon dioxide emissions from Tucuruí reservoir (Amazon biome): new findings based on three-dimensional ecological model simulations. **Science of the Total Environment**, v.551/552, p.676–694, 2016. Available from: <http://doi.org/10.1016/j.scitotenv.2016.02.001>.

CURTARELLI, M.P.; OGASHAWARA, I.; ALCÂNTARA, E.H.; STECH, J.L. Coupling remote sensing bio-optical and three-dimensional hydrodynamic modeling to study the phytoplankton dynamics in a tropical hydroelectric reservoir. **Remote Sensing of Environment**, v.157, p.185-198, 2015. Available from: <https://doi.org/10.1016/j.rse.2014.06.013>.

DADSON, S. J.; ASHPOLE, I.; HARRIS, P.; DAVIES, H. N.; CLARK, D. B.; BLYTH, E.; TAYLOR, C. M. Wetland inundation dynamics in a model of land surface climate: evaluation in the Niger inland delta region. **Journal of Geophysical Research Atmospheres**, v.115, p.1–7, 2010.

DEARDOFF, J. W. Convective velocity and temperature scales for unstable planetary boundary layer and for Rayleigh convection. **Journal of Atmospheric Sciences**, v.27, p.1211–1213, 1970.

DONLON, C. J.; MINNETT, P.; GENTEMANN, C.; NIGHTINGALE, T. J.; BARTON, I. J.; WARD, B. Towards improved validation of satellite sea surface skin temperature measurements for climate research. **Journal of Climate**, v. 15, n.4, p.353–369, 2002.

DUNNE, T.; MERTES, L. A. K.; MEADE, R. H.; RICHEY, J. E.; FORSBERG, B. Exchanges of sediment between the flood plain and channel of the Amazon River in Brazil. **Geological Society of America Bulletin**, v.110, n.4, p.450–467, 1998. DOI:10.1130/0016-7606(1998)110<0450:EOSBTF>2.3.CO;2.

DUNNE, T.; AALTO, R. E. Large river floodplains. In: SHRODER, J. F. (Ed.) **Treatise on geomorphology**. San Diego: Academic Press, 2013. p. 645–678.

EMERY, W.J.; CASTRO, S.; WICK, G.A.; SCHLUESSEL, P.; DONLON, C. Estimating sea surface temperature from Infrared satellite and in situ temperature data. **Bulletin of the American Meteorological Society**, v.82, p.2773–2786, 2001. Available from: [https://doi.org/10.1175/1520-0477\(2001\)082<2773:ESSTFI>2.3.CO;2](https://doi.org/10.1175/1520-0477(2001)082<2773:ESSTFI>2.3.CO;2).

ENGLE, D.; MELACK, J. M. Methane emissions from an Amazon floodplain lake: enhanced release during episodic mixing and during falling water. **Biogeochemistry**, v.51, p.71–90, 2000.

EVANS, M. A.; MACINTYRE, S.; KLING, G. W. Internal wave effects on photosynthesis: experiments, theory, and modeling. **Limnology and Oceanography**, v.53, n.1, p.339–353, 2008.

EUGSTER, W.; KLING, G.; JONAS, T.; MCFADDEN, J. P.; WUEST, A., MACINTYRE, S.; CHAPIN, F. S. CO<sub>2</sub> exchange between air and water in an Arctic Alaskan and midlatitude Swiss lake: importance of convective mixing. **Journal of Geophysical Research-Atmospheres**, v.108, n.D12, p.20, 2003. Available from: <http://doi.org/4362.10.1029/2002jd002653>.

FERREIRA, R. D.; BARBOSA, C. C. F.; NOVO, E. M. L. D. M. Assessment of in vivo fluorescence method for chlorophyll- a estimation in optically complex waters (Curuai floodplain , Pará – Brazil ). **Acta Limnologica Brasiliensia**, v.24, n.4, p.373–386, 2012. Available from: <http://doi.org/10.1590/S2179-975X2013005000011>.

GANF, G. G. Diurnal mixing and the vertical distribution of phytoplankton in a shallow Equatorial lake (Lake George, Uganda). **British Ecological Society**, v.62, p.611–629, 1974.

HEISKANEN, J. J.; MAMMARELLA, I.; HAAPANALA, S.; PUMPANEN, J.; VESALA, T.; MACINTYRE, S.; OJALA, A. Effects of cooling and internal wave motions on gas transfer coefficients in a boreal lake. **Tellus, Series B: Chemical and Physical Meteorology**, v.66, n.1, p.1–16, 2014. Available from: <http://doi.org/10.3402/tellusb.v66.22827>.

HESS, L. L.; MELACK, J. M.; AFFONSO, A. G.; BARBOSA, C.; GASTIL-BUHL, M.; NOVO, E. M. L. M. Wetlands of the lowland Amazon Basin: extent, vegetative cover, and dual-season inundated area as mapped with JERS-1 synthetic aperture radar. **Wetlands**, v.35, n.4, p.745–756, 2015. Available from: <http://doi.org/10.1007/s13157-015-0666-y>.

HICKS, B. B. A procedure for the formulation of bulk transfer coefficients over water. **Boundary-Layer Meteorology**, v.8, p.515–524, 1975.

HUNTER, N. M.; BATES, P. D.; HERRITT, M. S.; WILSON, M. D. Simple spatially-distributed models for predicting flood inundation: a review. **Geomorphology**, v.90, n.3/4, p.208–225, 2007.  
DOI:10.1016/j.geomorph.2006.10.021.

IMBERGER, J. Thermal characteristics of standing waters: an illustration of dynamic processes. **Hydrobiologia**, v.125, p.7–29, 1985.

JELLISON, R.S.; MELACK, J. M. Meromixis in hypersaline Mono Lake, California. 1: vertical mixing and density stratification during the onset, persistence, and breakdown of meromixis. **Limnology and Oceanography**, v.38, p.1008–1019, 1993.

KEMENES, A.; FORSBERG, B. R.; MELACK, J. M. CO<sub>2</sub> emissions from a tropical hydroelectric reservoir (Balbina, Brazil). **Journal of Geophysical Research: Biogeosciences**, v.116, n.3, p.1–11, 2011. Available from: <http://doi.org/10.1029/2010JG001465>.

KIM, J. W. A generalized bulk model of the oceanic mixed layer. **Journal of Physical Oceanography**, v.6, p.686–695, 1976.

LESACK, L. F. W.; MELACK, J. M. Flooding hydrology and mixture dynamics of lake water derived from multiple sources in an Amazon floodplain lake. **Water Resources Research**, v.31, n.2, p.329–345, 1995. DOI:10.1029/94WR02271.

LI, Z.L.; WU, H.; WANG, N.; QIU, S.; SOBRINO, J. A.; WAN, Z. Review article: land surface emissivity retrieval from satellite data. **International Journal of Remote Sensing**, 2013. Available from: <http://dx.doi.org/10.1080/01431161.2012.716540>.

LIVINGSTONE, D. M. Thermal structure of a large temperate central european lake. **Climatic Change**, v.57, n.1, p.205–225, 2003.

LOBO, F. L.; NOVO, E. M. L. D. M.; BARBOSA, C. C. F.; GALVÃO, L. S. Reference spectra to classify Amazon water types. **International Journal of Remote Sensing**, v.33, n.11, p.3422–3442, 2012. Available from: <http://doi.org/10.1080/01431161.2011.627391>.

LOMBARDO, C.; GREGG, M. Similarity scaling of viscous and thermal dissipation in a convecting surface boundary layer. **Journal of Geophysical Research**, v.94, n.C5, p.6273–6284, 1989.

MACINTYRE, S.; MELACK, J.M. Vertical mixing in Amazon floodplain lakes. **Verhandlungen des Internationalen Verein Limnologie**, v.22, p.1283–1287, 1984.

MACINTYRE, S.; MELACK, J.M. Frequency and depth of vertical mixing in an Amazon floodplain lake (L. Calado, Brazil). **Verhandlungen des Internationalen Verein Limnologie**, v.23, p.80-85, 1988.

MACINTYRE, S.; WANNINKHOF, R.; CHANTON, J. Trace gas exchange across the air-water interface in freshwater and coastal marine environments. In: MATSON, P.; HARRISS, R. (Ed.). **Biogenic trace gases**: measuring emissions from soil and water. Malden: Blackwell Science, 1995. p.52–97.

MACINTYRE, S.; ROMERO, J.; KLING, G. W. Spatial-temporal variability in surface layer deepening and lateral advection in an embayment of Lake Victoria, East Africa. **Limnology and Oceanography**, v.47, p.656–671, 2002.

MACINTYRE, S.; MELACK, J.M. Mixing dynamics in lakes across climatic zones. **Encyclopedia of Inland Waters**, v.2, p.603–612, 2009.

MACINTYRE, S.; FRAM, J. P.; KUSHNER, P. J.; BETTEZ, N. D.; BRIEN, W. J. O.; HOBBIE, J. E.; KLING, G. W. Climate-related variations in mixing dynamics in an Alaskan arctic lake. **Limnology and Oceanography**, v.54, n.6, pt 2, p.2401–2417, 2009. Available from: [http://doi.org/10.4319/lo.2009.54.6\\_part\\_2.2401](http://doi.org/10.4319/lo.2009.54.6_part_2.2401).

MACINTYRE, S.; JONSSON, A.; JANSSON, M.; ABERG, J.; TURNEY, D. E.; MILLER, S. D. Buoyancy flux, turbulence, and the gas transfer coefficient in a stratified lak. **Geophysical Research Letters**, v.37, p.2–6, 2010. Available from: <http://doi.org/10.1029/2010GL044164>.

MACINTYRE, S.; ROMERO, J. R.; SILSBE, G. M.; EMERY, B. M. Stratification and horizontal exchange in Lake Victoria, east Africa. **Limnology and Oceanography**, v.59, p.1805–1838, 2014.

MACINTYRE, S. **Thermistor chains** [mensagem pessoal]. Mensagem recebida por <cmr@bren.ucsb.edu> em 23 maio 2014.

MACKAY, M. D.; NEALE, P. J.; ARP, C. D.; DOMIS, L. N. D. S.; FANG, X.; GAL, G.; LITCHMAN, E. Modeling lakes and reservoirs in the climate system. **Limnology and Oceanography**, v.54, n.6, pt.2, p.2315–2329, 2009. Available from: [http://doi.org/10.4319/lo.2009.54.6\\_part\\_2.2315](http://doi.org/10.4319/lo.2009.54.6_part_2.2315).

MELACK, J. M.; KILHAM, P. Photosynthetic rates of phytoplankton in east African alkaline, saline lakes. **Limnology and Oceanography**, v.19, p.743–775, 1974.

MELACK, J. M.; FISHER, T. R. Diel oxygen variations and their ecological implications in Amazon floodplain lakes. **Archiv für Hydrobiologie**, v.98, p.422–442, 1983.

MELACK, J. M.; HESS, L.; GASTIL, M.; FORSBERG, B. R.; HAMILTON, S. K.; LIMA, I. B. T.; NOVO, E. M. L. M. Regionalization of methane emissions in the Amazon Basin with microwave remote sensing. **Global Change Biology**, v.10, n.5, p.530–544, 2004. Available from: <http://doi.org/10.1111/j.1529-8817.2003.00763.x>.

MELACK, J. M.; NOVO, E. M. L. D. M.; FORSBERG, B. R.; PIEDADE, M. T. F.; MAURICE, L. Floodplain ecosystem processes. **Amazonia and Global Change**, n.2003, p.576, 2009. Available from: <http://doi.org/10.1029/2008GM000721>.

MELACK, J. M.; COE, M. T. Climate change and the floodplain lakes of the Amazon basin. In: GOLDMAN, C. R.; KUMAGAI, M.; ROBARTS, R. D. **Climate change and inland waters: Impacts and Mitigation for Ecosystems and Societies**. New York: Wiley and Sons, 2013. Available from:

<https://doi.org/10.1002/9781118470596.ch17>.

MELACK, J. M. Aquatic ecosystems. In: NAGY, L.; FORSBERG, B.R.; ARTAXO, P. (Ed.). **Interactions between biosphere, atmosphere and human land use in the Amazon Basin**. Berlin, Heidelberg: Springer, 2016. p. 119–48.

MELO, S.; HUSZAR, V. L. M.; ROLAND, F.; ESTEVES, F. A.; BOZELLI, R. L. Phytoplankton diel variation and vertical distribution in two Amazonian floodplain lakes (Batata Lake and Mussura Lake, Para-Brasil) with different mixing regimes. **Amazoniana**, v.8, p.1–10, 2004.

MERTES, L. A K.; DANIEL, D. L.; MELACK, J. M.; NELSON, B.; MARTINELLI, A.; FORSBERG, B. R. Spatial patterns of hydrology, geomorphology, and vegetation on the floodplain of the Amazon River in Brazil from a remote sensing perspective. **Geomorphology**, v.13, p. 215–232, 1995. Available from: [http://doi.org/10.1016/0169-555X\(95\)00038-7](http://doi.org/10.1016/0169-555X(95)00038-7).

MONIN, A. S.; OBUKHOV, A. M. Basic laws of turbulent mixing in the surface layer of the atmosphere. **Contributions of the Geophysical Institute Academy of Science**, v.24, n.151, p.163–187, 1954.

MONISMITH, S. An experimental study of the upwelling response of stratified reservoirs to surface shear stress. **Journal of Fluid Mechanics**, v.171, p.407-439, 1986. DOI:10.1017/S0022112086001507.

NEHORAI, R.; LENSKY, N.; BRENNER, S.; LENSKY I. The dynamics of the skin temperature of the dead sea. **Advances in Meteorology**, v. 2013, n.296714, 2013.

NOVO, E. M. L. M.; BARBOSA, C. C. F.; FREITAS, R. M.; SHIMABUKURO, Y. E.; MELACK, J. M.; PEREIRA FILNHO, W. Seasonal changes in chlorophyll distributions in Amazon floodplain lakes derived from MODIS images. **Limnology**, v. 7, n. 3, p. 153–161, 2006. DOI: <10.1007/s10201-006-0179-8>. Available from: <<http://dx.doi.org/10.1007/s10201-006-0179-8>>.

PATTERSON, J. C. Modeling the effects of motion on the primary production of phytoplankton in the mixed layer of lakes. **Aquatic Sciences**, v.53, p.218–238, 1991.

PERNICA, P.; WELLS, M. G.; MACINTYRE, S. Persistent weak thermal stratification inhibits mixing in the epilimnion of north-temperate Lake Opeongo, Canada. **Aquatic Sciences**, v.76, n.2, p.187–201, 2014. Available from: <http://doi.org/10.1007/s00027-013-0328-1>.

PAREETH, S. et al. Warming trends of perialpine lakes from homogenised time series of historical satellite and in-situ data. **Science of the Total Environment**, v.578, p.417–426, 2016. Available from: <http://dx.doi.org/10.1016/j.scitotenv.2016.10.199>.

RAYNER, K. N. **Diurnal energetics of a diurnal surface layer**. Perth: University of Western Australia, 1981.

READ, J. S.; HAMILTON, D. P.; DESAI, A. R.; ROSE, K. C.; MACINTYRE, S.; LENTERS, J. D.; WU, C. H. Lake-size dependency of wind shear and convection as controls on gas exchange. **Geophysical Research Letters**, v.39, n.9, p.1–5, 2012. Available from: <http://doi.org/10.1029/2012GL051886>.

REINART, A.; REINHOLD, M. Mapping surface temperature in large lakes with MODIS data. **Remote Sensing of Environment**, v.112, n.2, p.603–611, 2008. DOI:10.1016/j.rse.2007.05.015.

RICHEY, J. E.; MELACK, J. M.; AUFDENKAMPE, A. K.; BALLESTER, V. M.; HESS, L. L. Outgassing from Amazonian rivers and wetlands as a large tropical source of atmospheric CO<sub>2</sub>, **Nature**, v.416, n.1991, p.6413–6416, 2002.

RILEY, W. J.; SUBIN, Z. M.; LAWRENCE, D. M. Barriers to predicting changes in global terrestrial methane fluxes: analyses using CLM4Me, a methane biogeochemistry model integrated in CESM. **Biogeosciences**, v.8, p.1925–1953, 2011.

RUDORFF, C. M.; MELACK, J. M.; MACINTYRE, S.; BARBOSA, C. C. F.; NOVO, E. M. L. M. Seasonal and spatial variability of CO<sub>2</sub> emission from a large floodplain lake in the lower Amazon. **Journal of Geophysical Research**, v.116, G04007, 2011.

RUDORFF, C. M.; MELACK, J. M.; BATES, P. D. Flooding dynamics on the lower Amazon floodplain: 1. hydraulic controls on water elevation, inundation extent, and river-floodplain discharge. **Water Resources Research**, v.50, p.619–634, 2014a. DOI:10.1002/2013WR014091.

RUDORFF, C. M.; MELACK, J. M.; BATES, P. D. Flooding dynamics on the lower Amazon floodplain: 2. seasonal and interannual hydrological variability. **Water Resources Research**, v.50, Jan. 2014b. Available from: <http://doi.org/10.1002/2013WR014714>.

RUDORFF, C. M.; DUNNE, T.; MELACK, J. M. Recent increase of river-floodplain suspended sediment exchange in a reach of the lower Amazon River. **Earth Surface Processes and Landforms**, v.43, p.322–332, 2018. DOI:10.1002/esp.4247. Available from: <http://doi.wiley.com/10.1002/esp.4247>.

SAHOO, G. B.; SCHLADOW, S. G. Impacts of climate change on lakes and reservoirs dynamics and restoration policies. **Sustainability Science**, v.3. n.2, p.189–199, 2008. Available from: <http://doi.org/10.1007/s11625-008-0056-y>.

SAMUELSSON, P.; KOURZENEVA, E.; MIRONOV, D. The impact of lakes on the European climate as simulated by a regional climate model. **Boreal Environment Research**, v.15, n.2, p.113–129, 2010.

SANDER DE CARVALHO, L. A.; BARBOSA, C.C.F.; NOVO, E. M. L. DE M., RUDORFF, C. DE M. Implications of scatter corrections for absorption measurements on optical closure of Amazon floodplain lakes using the Spectral Absorption and Attenuation Meter (AC-S-WETLabs). **Remote Sensing of Environment**, v.157, p.123–137, 2015. Available from: <http://doi.org/10.1016/j.rse.2014.06.018>.

- SANDER DE CARVALHO, L. A. **Bio-optical characterization of Amazon floodplain lakes and evaluation of the retrieval of optically active constituent using remote sensing**. 2016. 201 p. Thesis (Doctor in Remote Sensing) - Instituto Nacional de Pesquisas Espaciais (INPE), São José dos Campos, 2016. Available: <<http://urlib.net/8JMKD3MGP3W34P/3LRECPB>>.
- SAVTCHENKO, A.; OUZOUNOV, D.; AHMAD, S.; ACKER, J.; LEPTOUKH, G.; KOZIANA, J.; NICKLESS, D. Terra and aqua MODIS products available from NASA GES DAAC. **Advances in Space Research**, v.34, p.710-714, 2004.
- SCOFIELD, V.; MELACK, J. M.; BARBOSA, P. M.; AMARAL, J. H. F.; FORSBERG, B. R.; FARJALLA, V. F. Carbon dioxide outgassing from Amazonian aquatic ecosystems in the Negro River basin. **Biogeochemistry**, v.129, p.77–91, 2016. Available from:<https://doi.org/10.1007/s10533-016-0220-x>.
- SIPPEL, S. J.; HAMILTON, S. K.; MELACK, J. M. Inundation area and morphometry of lakes on the Amazon River floodplain, Brazil. **Archiv für Hydrobiologie**, v.123, n.4, p.385–400, 1992.
- SUBIN, Z. M.; RILEY, W. J.; MIRONOV, D. An improved lake model for climate simulations: model structure, evaluation, and sensitivity analyses in CESM1. **Journal of Advances in Modeling Earth Systems**, v.4, p.1–27, 2012.
- TALLING, J. F. The incidence of vertical mixing, and some biological and chemical consequences, in tropical African lakes. **Verhandlungen der Internationalen Vereinigung Limnologie**, v.17, p.998-1012, 1969.
- TALLING, J. F.; LEMOALLE, J. **Ecological dynamics of tropical inland waters**. New York: Cambridge University Press, 1998. 441p.
- TEDFORD, E. W.; MACINTYRE, S.; MILLER, S. D.; CZIKOWSKY, M. J. Similarity scaling of turbulence in a temperate lake during fall cooling. **Journal of Geophysical Research: Oceans**, v.119, 2014.

TERRAY, E.; DONELAN, M.; AGRAWAL, Y.; DRENNAN, W.; KAHMA, K.; WILLIAMS, A.; HWANG, P.; KITAIGORODSKII, S. Estimates of kinetic energy dissipation under breaking waves. **Journal of Physical Oceanography**, v.26, n.5, p.792–807, 1996.

THIEMANN, S.; SCHILLER, H. Determination of the bulk temperature from NOAA/AVHRR satellite data in a midlatitude lake. **International Journal of Applied Earth Observation and Geoinformation**, v.4, p.339–349, 2003.

TRIGG, M. A.; BATES, P. D.; WILSON, M. D.; SCHUMANN, G.; BAUGH, C. Floodplain channel morphology and networks of the middle Amazon River. **Water Resources Research**, v.48, W10504, 2012. DOI:10.1029/2012WR011888.

TUNDISI, J. G.; FORSBERG, B. R.; DEVOL, A. H.; ZARET, T. M.; TUNDISI, T. M.; DOS SANTOS, A.; RIBEIRO, J. S.; HARDY, E. R. Mixing patterns in Amazon lakes. **Hydrobiologia**, v.108, p.3–15, 1984.

VALÉRIO, A. M.; KAMPEL, M.; ASSIREU, A.T.; STECH, J.L. The asymmetric fragmentation operator applied to meteo-limnological time series in a tropical reservoir. **Ecological Informatics**, v.8, p.29-36, 2012. Available from: <https://doi.org/10.1016/j.ecoinf.2011.12.003>.

XING, Z.; FONG, D. A.; LO, E. Y.; MONISMITH, S. G. Thermal structure and variability of a shallow tropical reservoir. **Limnology and Oceanography**, v.59, p.115–128, 2014.

WAN, Z.; HOOK, S.; HULLEY, G. **MYD11A1 MODIS/Aqua land surface temperature/emissivity daily L3 global 1km SIN Grid V006**. Washington: NASA, 2015. DOI: 10.5067/MODIS/MYD11A1.006.

WEYHENMEYER, G. A.; MACKAY, M.; STOCKWELL, J. D.; THIERY, W.; GROSSART, H.P.; AUGUSTO-SILVA, P. B.; WOOLWAY, R. I. Citizen science shows systematic changes in the temperature difference between air and inland waters with global warming. **Scientific Reports**, v.7, 2017. Available from: <http://doi.org/10.1038/srep43890>.

ZAPPA, C. J.; MCGILLIS, W. R.; RAYMOND, P. A.; EDSON, J. B.; HINTSA, E. J.; ZEMMELINK, H. J.; DACEY, J. W. H.; HO T. Environmental turbulent mixing controls on air-water gas exchange in marine and aquatic systems.

**Geophysical Research Letters**, v.34, L10601, 2007. DOI:10.1029/2006GL028790.